



RESEARCH ARTICLE

10.1029/2023JD039906

An Independent Evaluation of GHGSat Methane Emissions: Performance Assessment

Key Points:

- GHGSat methane precision was found to be 1%–5%, varying with surface reflectance, terrain variability, and solar zenith angle
- GHGSat methane detection limit can be as low as 100 kg/hr under ideal conditions, but more typically is about 200 kg/hr
- GHGSat performance was found to be generally consistent with that reported by the company

C. A. McLinden^{1,2} , Debora Griffin¹ , Zoe Davis^{1,3}, Colin Hempel^{1,4}, James Smith^{1,5}, Christopher Sioris¹, Ray Nassar⁶ , Omid Moeini^{6,7}, Eric Legault-Ouellet⁸ , and Alain Malo⁸

¹Air Quality Research Division, Environment and Climate Change Canada, Toronto, ON, Canada, ²Department of Physics and Engineering Physics, University of Saskatchewan, Saskatoon, SK, Canada, ³Environmental Protection Branch, Environment and Climate Change Canada, Toronto, ON, Canada, ⁴Department of Physics & Astronomy, University of British Columbia, Vancouver, BC, Canada, ⁵Department of Physics, University of Waterloo, Waterloo, ON, Canada, ⁶Climate Research Division, Environment and Climate Change Canada, Toronto, ON, Canada, ⁷Now at Natural Resources Canada, Canadian Forest Service, Victoria, BC, Canada, ⁸Canadian Meteorological Centre, Environment and Climate Change Canada, Montreal, QC, Canada

Correspondence to:

C. A. McLinden,
chris.mclinden@ec.gc.ca

Citation:

McLinden, C. A., Griffin, D., Davis, Z., Hempel, C., Smith, J., Sioris, C., et al. (2024). An independent evaluation of GHGSat methane emissions: Performance assessment. *Journal of Geophysical Research: Atmospheres*, 129, e2023JD039906. <https://doi.org/10.1029/2023JD039906>

Received 6 SEP 2023
Accepted 15 JUL 2024

Author Contributions:

Conceptualization: C. A. McLinden
Data curation: C. A. McLinden, Debora Griffin, Ray Nassar, Omid Moeini, Eric Legault-Ouellet, Alain Malo
Formal analysis: C. A. McLinden, Colin Hempel, James Smith, Christopher Sioris
Investigation: Debora Griffin
Methodology: C. A. McLinden, Debora Griffin, Zoe Davis, Colin Hempel, James Smith, Christopher Sioris, Ray Nassar, Omid Moeini
Resources: C. A. McLinden, Debora Griffin
Software: C. A. McLinden, Debora Griffin, Zoe Davis, Colin Hempel, James Smith, Christopher Sioris,

Abstract An independent evaluation of methane emissions data from GHGSat, a private company that operates a constellation of small microsatellites flying Fabry-Perot spectrometers operating at 1.6 μm , was performed. Data from multiple GHGSat commercial satellites, consisting of retrieved methane, diagnostics, and, where detected, plume and emissions information from roughly 250 scenes across Canada were analyzed. From these, 10 scenes contained methane plumes with a 2% detection rate for oil and gas scenes, and 10% for landfills. Methane precision was found to be 5%/2% on average for the C1/C2–C5 designs, with some variability due to scene albedo, terrain roughness, and airmass. Synthetic GHGSat plumes, generated using Lagrangian plume dispersion model and GHGSat characteristics, indicates typical detection limits of 240/180 kg/hr (C1/C2–C5), with a best case of roughly 100 kg/hr. Emissions and their uncertainties calculated using an alternative approach were in broad agreement with GHGSat-reported emissions. Overall, the performance of the GHGSat C2 design (also used for C3 onward) for favorable-viewing conditions was found to be largely consistent with company-advertised performance.

Plain Language Summary We performed an independent evaluation of methane emissions data from GHGSat, a private company that owns and operates its own group of satellites, in order to evaluate the precision of their methane data products and compare these findings with that advertised. Roughly 250 GHGSat data scenes were acquired with 10 plumes detected, 2 for oil and gas and 8 for landfills. These, combined with advanced plume models, statistical analyses, and alternative data processing software, were used in the evaluation. It was found that the GHGSat-reported detection limit—the quantity of methane release that was is the edge of detectability—of 100 kg/hr was possible, but only for ideal conditions. Ideal in this case means a surface that is quite reflective (at the wavelengths detected by the GHGSat sensors, roughly 1.6 μm) and flat near the source of the emissions. A detection limit of 180 kg/hr is more representative of average conditions.

1. Introduction

Reducing methane emissions is seen as the most straightforward way of minimizing climate change in the short term. Over a 20 years time frame methane is roughly 80 times more potent a greenhouse gas compared to carbon dioxide (or 30 times over a 100 years time frame) (Forster et al., 2021).

As part of the Global Methane Pledge, Canada has indicated that it will reduce methane emissions by at least 35% below 2020 levels by the year 2030 (Environment and Climate Change Canada, 2022). Complicating this, however, is that Canadian anthropogenic methane emissions remain quite uncertain, with total annual amounts varying by nearly a factor of two, from 3.7 to 7 Tg/yr. Bottom-up (or activity-based) inventories are typically on the lower end and top-down (or atmospheric concentration-based) on the higher end (Baray et al., 2021; Lu et al., 2022). Much of this uncertainty comes from the oil and gas sector, due to complex operations, variable reporting requirements across different jurisdictions, incomplete monitoring, and methane leaks (Atherton et al., 2017; Baray et al., 2018; Chan et al., 2020; Conrad et al., 2023; Festa-Bianchet et al., 2023; Johnson et al., 2017, 2023a; MacKay et al., 2021; Tyner & Johnson, 2021; Zavala-Araiza et al., 2018).

© 2024 His Majesty the King in Right of Canada. Reproduced with the permission of the Minister of Environment And Climate Change Canada. This is an open access article under the terms of the [Creative Commons Attribution-NonCommercial License](https://creativecommons.org/licenses/by/4.0/), which permits use, distribution and reproduction in any medium, provided the original work is properly cited and is not used for commercial purposes.

Omid Moeini, Eric Legault-Ouellet,
Alain Malo

Supervision: C. A. McLinden,
Debora Griffin

Writing – original draft: C. A. McLinden

Writing – review & editing:

C. A. McLinden, Debora Griffin,
James Smith, Christopher Sioris,
Ray Nassar, Omid Moeini

A key piece of Canada's strategy to achieve this ambitious goal is the utilization of Satellite Earth Observations (SEO) of methane (Environment and Climate Change Canada, 2022). Instruments such as SCIAMACHY (SCanning Imaging Absorption SpectroMeter for Atmospheric CHartographY) (Buchwitz et al., 2005), GOSAT/GOSAT2 (Greenhouse Gases Observing Satellite) (Yoshida et al., 2011), and more recently, TROPOMI (Tropospheric Monitoring Instrument) (Lorente et al., 2021) have demonstrated that SEO can provide methane column average mixing ratios at precisions of 1% or better. These instruments observe in the short-wave infrared spectrum, taking advantage of methane absorption bands near 1.6 and/or 2.2 μm where surface-reflected sunlight provides the signal. With new sensors such as MethaneSat (Hamburg et al., 2022) soon coming online the volume of data is expected to grow considerably.

For Canada and other nation committed to the Global Methane Pledge, it will be important to utilize all available SEO resources to better quantify emissions, and critical here is to understand the strengths and limitations of each instrument, including those from government agencies, non-profits, and, increasing, the private sector. Indeed, developments in technology, computing power, and access to space now mean it is possible for methane sensors to be deployed on nanosatellites and microsatellites, making it feasible for private industry to develop and launch their own satellites for commercial monitoring. The focus of this paper is to evaluate the performance from one such company, GHGSat. Performance here refers to the technical characteristics of the GHGSat products such as the precision of the methane data itself, an evaluation of the emissions algorithm and its uncertainties, and quantifying the emissions detection limit. Placing these in an observing system context by considering the issues of observability and completeness (Jacob et al., 2022) is beyond the scope of this work and will be addressed in a follow-up publication.

2. GHGSat

GHGSat is a private Canadian company that develops (with industrial partners), owns, operates, and analyzes data from a constellation of small microsatellites observing atmospheric methane at high spatial resolution for the purpose of methane emissions monitoring (GHGSat, 2024). Their initial demonstrator satellite was launched in 2016 (Jervis et al., 2021), with commercial follow-ons in 2020, 2021, 2022, and 2023. Their business model is primarily subscription-based where clients pay for observations made over a selected location, although a smaller fraction of their observations are made available for research purposes.

GHGSat currently has 12 satellites in orbit, 11 of which are designed to detect methane (one targeting CO_2) with some key particulars summarized in Table 1 (largely restating and expanding upon information from Jervis et al. (2021)). All GHGSat platforms collect short wave infrared spectra using a wide-angle Fabry-Perot imaging spectrometer that operates in target mode. This particular design provides spectra at high spatial resolution, 25 m, and moderate spectral resolution, 0.1 nm, over a 12×15 km scene. Information on the original demonstration instrument, GHGSat-D, is published (Jervis et al., 2021). Its successors, GHGSat C1–C11 (hereafter simply referred to as C1, C2, C3, ...) are similar but with improvements. Details on the precise nature of these improvements are not publicly available but broadly speaking are related to quality of the detectors and filters, improvements to stray light and ghosting, and using an lower F/# to increase signal. C2–C5 are the same basic design as C1 but further incorporate an order-selecting filter. As such the initial expectation is that the performance of C2–C5 will all be similar, with some differences between them and C1. C6–C9 and C11 are believed to be the same design as C2–C5.

2.1. Data Processing and Methane Retrievals

A scene is derived from roughly 200 successive, overlapping circular images. By adjusting its attitude, the instrument can remain pointing toward the target for the time required to obtain these images, roughly 20 s. Fabry-Perot spectrometers, as used here, differ from other types of spectrometers in that any given image contains a mix of spatial and spectral information, with the specific wavelength being a function of radial distance from the center of the image (wavelength decreases with increasing radius). Thus obtaining a spectrum for each pixel requires a series of images where each location on the ground is observed at multiple angles. To disentangle this complex mix of spatial and spectral information, images are corrected, aligned, and ultimately geo-located. See Jervis et al. (2021) for additional information.

The methane mixing ratio and the 1.6 μm surface reflectivity are retrieved from the spectra using a two-step optimal estimation (Rogers, 2000) approach. In the first step a scene-wide absolute column-averaged methane

Table 1
Characteristics of the GHGSat Methane-Detecting Platforms

Satellite	
Satellite mass (kg)	15
Satellite size (cm ³)	20 × 30 × 40
Launch dates	D: June 2016
	C1: September 2020
	C2: January 2021
	C3–C5: May 2022
	C6–C8: April 2023
Orbit	
	Sun-synchronous, 500 km
Local time at descending node	D: 09:30
	C1–C2: 10:30
	C3–C5: 13:00
	C6–C9, C11: unknown
Instrument	
Instrument size (cm ³)	12 × 12 × 25
Spectrometer type	Wide angle Fabry-Perot etalon
Scene size (along × cross-track, km)	15 × 12
Spectral range, resolution (nm)	1,630–1,675, 0.1
Spatial resolution (m)	D: 50
	Others: 25
SNR (per-pixel)	D: 200 ^a
	Others: unknown
Scenes per orbit (per satellite)	1

^aPer-pixel signal for a 0.2 albedo scene and solar zenith angle of 40° divided by the shot noise, dark noise, and read noise (Jervis et al., 2021).

mixing ratio (in ppb) is retrieved using a full retrieval in which the Jacobian is evaluated for each iteration using the full forward model. Once complete, a linearized forward model is used to derive the departure of methane in each pixel from the scene-wide average, yielding the (column-averaged) excess methane. This simplified approach, which will tend to underestimate large departures from the mean, is done as performing full retrievals for each of the $\sim 2 \times 10^5$ pixels in a scene is too computationally expensive.

To better illustrate the nature of the GHGSat data to be examined in this study, an example of reflectivity and excess methane are shown in Figure 1 for a scene over the Windsor-Essex landfill in Southern Ontario on 10 December 2021 from C2. Reflectivity, or albedo, tends to vary from just above zero over water to 0.1–0.3 over various vegetation, and can occasionally exceed 0.35 at some locations in Canada (see Figure B2). When snow is present the albedo is around 0.1 (see Figure B3). GHGSat spatial resolution is sufficient to resolve smaller water bodies, roads, structures, and separate fields. Overall, this represents a fairly typical scene in terms albedo (an average value of 0.21 over this scene—no snow is present on this day).

The plume in the center of the scene (panel b) is quite apparent. Excess methane, which represents the difference from the scene-wide average, tends to fluctuate about zero due to errors, as can be seen in Figures 1b and A1b, due to random errors. Plumes appear as coherent enhancements if there is sufficient methane to overcome noise. In this example, the scene precision of the excess methane was calculated (see Section 3.1) at 1.7%. Here a relatively large plume was detected emanating from the landfill at the center of the scene and its direction was found to be consistent with winds from the Canadian weather forecast model, Global Environmental Multiscale model (GEM), 240°. The GHGSat reported emissions were 2,091 kg/hr \pm 51%.

Reported error and a quality flag are given in Figures 1c and 1d, respectively. Reported methane uncertainties vary over the scene in the range of 1%–2%, with some larger values along the edge. Note that 1% represents about 19 ppb.

2.2. Emissions Detection and Quantification

The first step in the analysis of a scene is to determine if one (or more) methane plumes are present, and if so, to isolate them from the background. The scene in Figure 1 was chosen as it has a distinct plume. In other cases however it is not a straightforward task to define it. This is based on several factors: the magnitude of emissions, the precision of the methane data, and wind speed. Also important to consider is the presence of any artifacts (e.g., albedo) which could be misidentified as, or obscure, a plume. Isolating a plume can be accomplished by either subtracting a background level of methane from all pixels in the vicinity of the plume (such that those not in the plume are essentially zero), or by explicitly separating the plume pixels from the background pixels.

GHGSat employs a plume identification and masking algorithm. One approach, described in Varon et al. (2018), involves first comparing a 5 × 5 block of pixels to a sample distribution from an upwind portion of the scene. If the distribution within a block is statistically different at the 95% confidence level, these pixels are assigned to the plume. This is followed by a median filter and then a Gaussian filter as demonstrated on synthetic plume data and described more thoroughly in Varon et al. (2018). Its replication was attempted on the plumes analyzed in this work, but a few false positives always remained. Other papers using GHGSat data describe variants of this approach, and it is not clear precisely what was used here and if additional manual filtering was required.

Several different methods have been identified for the retrieval of point source GHG emissions from space (Jacob et al., 2022; Nassar et al., 2017; Varon et al., 2018). All have their advantages and disadvantages, require information about the local wind speed and, directly or indirectly, quantify the flux. One common approach used for methane emissions is the so-called integrated mass (or methane) enhancement (IME) (Frankenberg et al., 2016). This method determines the total mass of the emissions downwind from the source within a certain area or

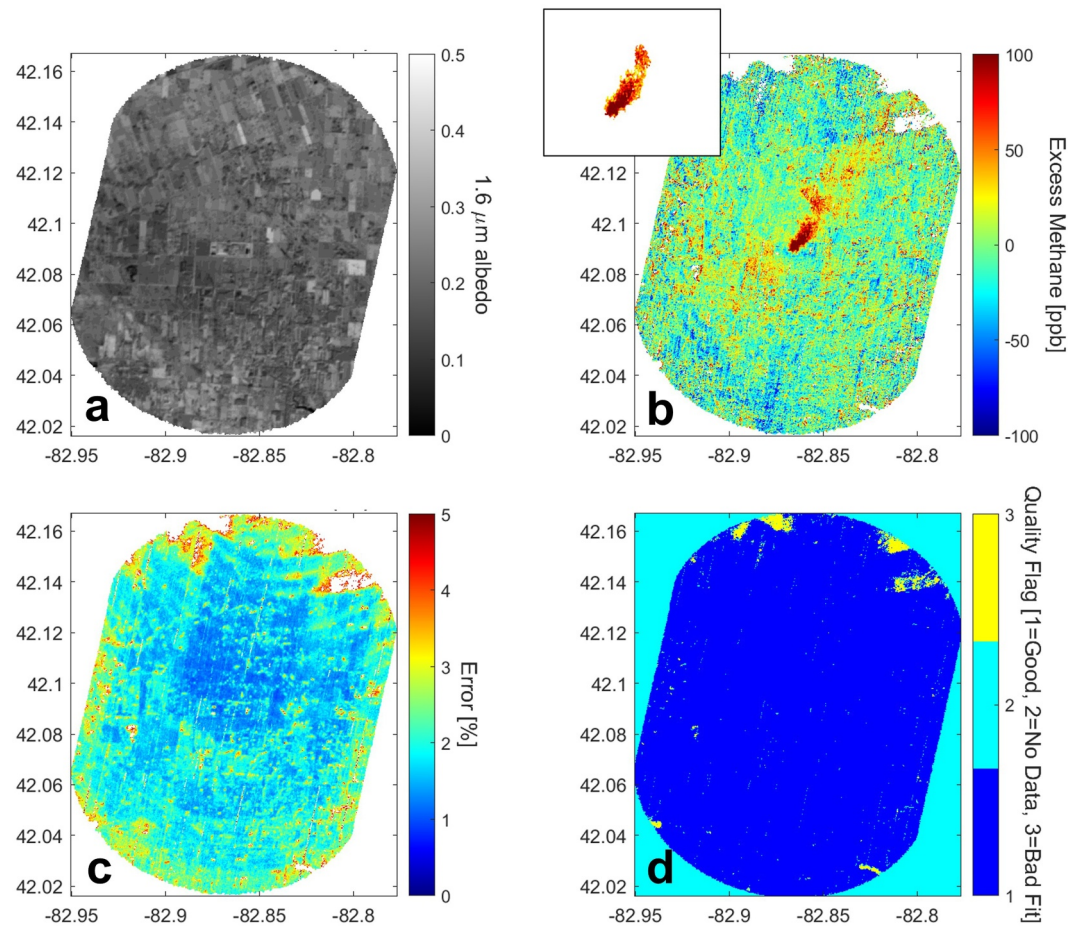


Figure 1. Data layers for a scene over the Essex-Windsor Landfill, taken on 10 December 2021, 15:23 UTC (09:52 LST) from GHGSat-C2: (a) the 1.6 μm reflectivity, (b) Excess methane, (c) Reported error of the excess methane, and (d) quality flag. A plume was identified in this scene, shown masked inset in panel (b). The GHGSat-inferred emission rate was $2,091 \text{ kg/hr} \pm 51\%$.

bounding box, with the size of the area governed by the wind speed. Following Adams et al. (2019), the emission rate Q is related to the mass inside the box by $Q = m/t_c$ (in the limiting case of no physical or chemical loss) where t_c is the residence time of the plume in the box. The residence time is related to the downwind distance through the wind speed. If a plume mask is used to differentiate between pixels in the plume and background then the box simply corresponds to the masked pixels.

Varon et al. (2018) developed a variant of the IME method to derive emissions from simulated GHGSat data. A cross-sectional flux method was also developed, but it is the IME method that was used to derive the emissions provided to ECCC. It is believed to be very similar to that documented in Varon et al. (2018) and differences, if known, will be pointed out here. The GHGSat IME approach is summarized by the following,

$$Q = \frac{U_{\text{eff}}}{L} \sum_{j=1}^N \Delta\Omega_j \cdot A_j \quad (1)$$

where U_{eff} (m/s) is an effective wind speed, L (m) is a characteristic length of the plume, $\Delta\Omega_j$ is the excess methane of pixel j (converted into mass per unit area), and A_j (m^2) is the area of pixel j . The summation is over all pixels identified to be in the plume and represents the mass of methane in the plume.

Varon et al. (2018) considered the quantities U_{eff} and L as operational parameters, with L taken as the square-root of the plume area, $L = \sqrt{A}$. This left U_{eff} , which was related to the 10 m wind speed, U_{10} (m/s), a physical quantity

that can be observed directly or obtained from a meteorological forecast or reanalysis system. The nature of the $U_{\text{eff}} = f(U_{10})$ relationship was derived using plume simulations from the Weather Research and Forecasting model in Large-eddy simulation mode (WRF-LES), with Gaussian noise added to reflect random errors in the excess methane field (Varon et al., 2018). Applying the same detection/masking and IME algorithms to WRF-LES simulated plumes, a relationship was derived relating the two by requiring the retrieved emission match the input values. This is done for a range of meteorological conditions, input emission rates, and methane precisions.

The precise $U_{\text{eff}} = f(U_{10})$ relationship was not provided. However, an analysis of the scenes with plumes, their associated emission rates and 10 m wind speeds allowed for the extraction of the operational relationship:

$$U_{\text{eff}} = b_1 + b_2 \cdot U_{10} \quad (2)$$

where $b_1 = 0.40$ and $b_2 = 0.35$. Thus the effective wind speed is usually smaller than the 10 m wind speed. The physical basis for this is difficult to understand and this is one of the drawbacks of the method. It could be related to the height of the wind—perhaps if a single, representative wind height is being used, it could be lower than 10 m (where wind speed would be smaller). Regardless, one advantage of this method is that, to the extent WRF-LES is able to simulate realistic plumes, it acts as a “calibration” in that systematic effects are accounted for.

The $U_{\text{eff}}-U_{10}$ relationship depends on the spatial resolution and precision of the instrument, and on the plume masking procedure, which requires customized plume modeling and fitting (Cusworth et al., 2019). This may explain the different GHGSat IME $U_{\text{eff}}-U_{10}$ relationships found in the literature. Varon et al. (2018) found $U_{\text{eff}} = b_1 + b_2 \cdot \log U_{10}$ worked best for GHGSat-D. Maasakkers et al. (2022) used Equation 2 to derive emissions from C1 and C2 scenes at large international landfills with $b_1 = 0.42$ and $b_2 = 0.34$, virtually identical to that derived from the data used here. One unanswered question is the extent to which this relationship varies with location, season, terrain, and other factors.

2.3. Survey of GHGSat Scenes Acquired by ECCC

Through several initiatives, including an opportunity through a joint European Space Agency (ESA)—Canadian Space Agency (CSA) initiative (European Space Agency, 2023), ECCC has acquired (via purchase, contract, ESA/CSA, or other) 249 GHGSat scenes between 2020 and 2022. Each scene delivered passed a screening for clouds and aerosols. Roughly one-quarter of the scenes were obtained through the ESA project, and three-quarters were from three different contracts or agreements between GHGSat and ECCC/Government of Canada. These targeted locations were either requested by ECCC (largely based on locations reporting substantial emissions) or selected by GHGSat using a proprietary artificial intelligence system that folded in additional satellite observations to assess where to observe. Beyond this there were an additional 4 scenes provided by GHGSat from their archives, chosen as they contain plumes.

Each data scene as provided to ECCC consists of the following files:

1. GeoTIFF image of excess methane (ppb)
2. GeoTIFF image of 1.6 μm reflectivity
3. GeoTIFF image of methane uncertainty (%)
4. GeoTIFF image of data quality flag (1 = good, 2 = no data, and 3 = bad)
5. json meta data file
6. (if plume detected) GeoTIFF image of excess methane, masked to only include the plume (ppb)
7. (if plume detected) Emissions summary file (Location, emissions rate, emissions uncertainty, and wind speed)

Files 6 and 7 are only provided if a plume is identified within the scene. Each GeoTIFF contains about $1,065 \times 865$ elements, with roughly 620×480 pixels making up the rounded-rectangle containing the data. For the example in Figure 1, there are roughly 250,000 pixels.

The scene-wide, or absolute, methane value was not provided and thus it cannot be evaluated for accuracy. Given that GHGSat does not observe spectra in an O_2 -band to constrain the local air column like most other GHG satellite missions, larger errors are likely in the column-averaged mixing ratio. However, due to the nature of the retrieval, it is expected that the excess methane values (and hence emissions) would be largely immune to errors in

the scene average. That is, a 10% underestimate of the scene-wide methane—which would constitute a rather poor observation—would yield at worst a 10% underestimate of excess methane, but more likely a smaller underestimate. Either way, this will not be the dominant source of error in the emission rate.

Likewise, there is no specific diagnostic information provided as to why some pixels were flagged as “bad.” Some of the possible general reasons communicated to the authors include low albedo or low signal.

A map showing the location of all scenes, aside from six scenes made at a concentrated animal feeding operation in Weld County, Colorado (40.36°, −104.50°), is shown in Figure 2. Also shown are the locations of all facilities reporting methane emissions to the 2022 Canadian GHG Reporting Program (GHG-RP) (Environment and Climate Change Canada, 2023b). The breakdown of scenes by satellite is given in Table 2.

Figure 3 shows the distribution of scenes as a function of source type (as defined by GHGSat). The two types with the most scenes are Wells (upstream oil and gas sector) and Waste (landfills). Of the 147 total oil and gas scenes (well and midstream), only 3 had confirmed plumes, with one maybe. Here, “maybe” is the term used by GHGSat (presumably) to denote an inconclusive detection, and for simplicity it is used without quotations for the remainder of this study. In these instances presumably a plume was detected but that one or more quality checks were not passed ultimately leading to a reduced confidence. No information about this is provided although visually, plumes designated as maybe appear noisier.

The waste category had 7 plumes with 3 maybes. It should be noted that 2 of the plumes both these category were hand-picked by GHGSat and not part of the regular data initiatives. They were provided to augment the number of plumes available for analysis and should not be considered in an analysis of detection rate. This is the reason the numbers used in Section 4.5 are slightly different.

3. GHGSat Evaluation Strategy and Tools

This work examines several facets of GHGSat scenes, including the precision of the (excess) methane data, emissions precision, uncertainties, and detection limits.

3.1. Methane Precision

In quantifying the methane precision for a given scene it is assumed that the variability in excess methane is dominated by random errors from the instrument, retrieval, or both. Examining Figure 1b, which shows the individual 25 m pixels, one can see that it is common for pixels in close proximity to vary by 25–50 ppb, on spatial scales smaller than the variability in albedo from Figure 1a, which lends support to this assumption. The histogram of excess methane for the Essex-Windsor landfill scene from Figure 1b is shown in Figure 4a. Even with the relatively large plume in this scene, the histogram appears symmetric about zero. The most straightforward estimate of precision, therefore, is simply the standard deviation of this distribution, 36 ppb or 1.9% of the total methane, assuming a background of 1,900 ppb (NOAA, 2024).

Alternatively, the fact that there may be real variability of methane or a bias that varies more slowly in space can be accounted for by instead considering the standard deviation over a 2 × 2 km box within the scene, chosen as

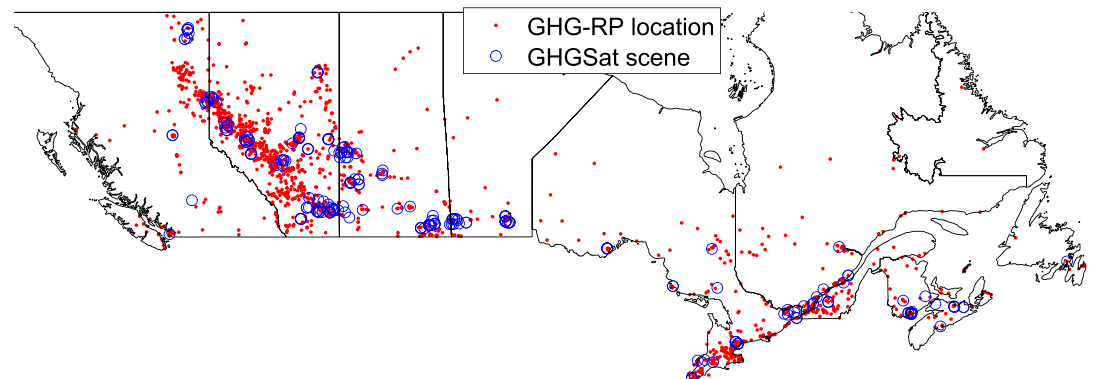


Figure 2. Location of GHGSat scenes and methane emission locations reporting to the 2020 Canadian GHG-RP.

Table 2
Breakdown of Scenes and Plumes Detection by GHGSat Satellite

Satellite	Total scenes	Scenes with plumes:	
		Confirmed	Maybe
C1	101	1 (0)	3
C2	87	8 (5)	1
C3	23	1	0
C4	17	0	0
C5	21	0	0
Total	149	10 (6)	4

Note. The numbers in brackets indicate the number of scenes with a plume but omitting the GHGSat hand-picked scenes provided to ECCC.

this is the approximate spatial extent of a plume. This box is then moved throughout the scene. The distribution of these individual 2×2 km standard deviations is shown in Figure 4b. The longer tail may be indicative of some areas with real variability, the edges of the scenes which tend to have greater variability, or contain some terrain-influenced biases. In this case the precision is taken as the median, 31 ppb or 1.8%, slightly smaller than the simpler approach. Note that going to even smaller boxes, say 500 m, does not appreciably lower this result, which also supports the notion that the observed variability is largely random. Further, choosing the median ensure that any real variability reflected in the tail does not have a significant influence on the result.

Scene precision was calculated in this way for all 249 scenes. These results are compared against the uncertainty from GHGSat, averaged over the scene, in Figure 5. The GHGSat uncertainty is a result from their optimal estimation methane retrieval (Section 2.1) and so it too represents a measure of random

error, although we will use their term “uncertainty” when referring to it. For satellites C2–C5 there is a fair degree of consistency as most points are close to the 1:1 line with both metrics indicating a precision between 1% and 5%. This may indicate that the instrument or error model used in the optimal estimation retrieval is appropriate. For C1 differences are larger with the calculated precision typically larger than the reported uncertainties, sometimes by 5% or more. It is unclear why there is this larger difference. Also of note is the fact that overall the calculated C1 precision is a factor of two or more larger than the others, typically in the 3%–10% range.

It was found that scene precision is determined in large part by three main parameters: scene reflectivity, variability of terrain height, and solar zenith angle (or airmass). In an attempt to parameterize this relationship, precision from the 249 scenes, σ (in %), was fit to the following function,

$$\sigma = a_1 + \left(a_2 \cdot \mu + \frac{a_3}{\mu} \right) + a_4 \cdot \lambda + a_5 \cdot z \quad (3)$$

where a_i are fitted constants, $\mu = \cos \theta_0$, θ_0 is the solar zenith angle, λ is the $1.6 \mu\text{m}$ scene albedo, and z is the terrain height variability (in km, defined as the standard deviation of terrain height across a scene). The GHGSat viewing zenith angles (VZAs) are always small, $<20^\circ$, and so the VZA term that might be considered in Equation 3, $1/\cos(\text{VZA})$, would only vary between 1 and 1.06 which would largely act as a constant. In the end it was found to not be important and therefore the dependency on airmass can be captured solely in terms of the solar zenith angle. The linear and inverse dependency on μ was chosen to allow for precision to increase or decrease with pathlength. Quantifying precision in this way allows it to be predicted for locations have not been observed

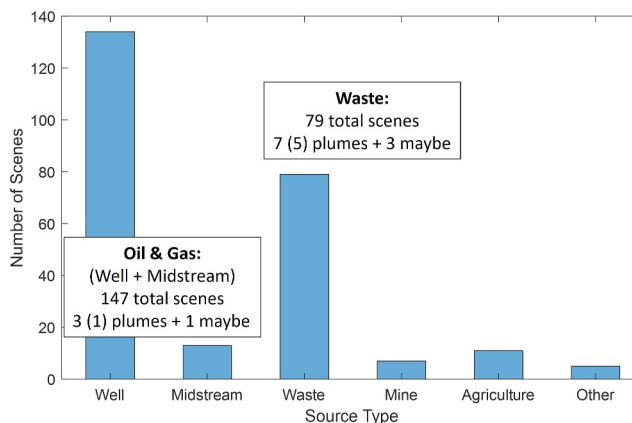


Figure 3. Breakdown of scenes by source type. Also indicated are the number scenes in which a plumes was detected. The numbers in brackets indicate the number of scenes with a plume but omitting the GHGSat hand-picked scenes provided to Environment and Climate Change Canada.

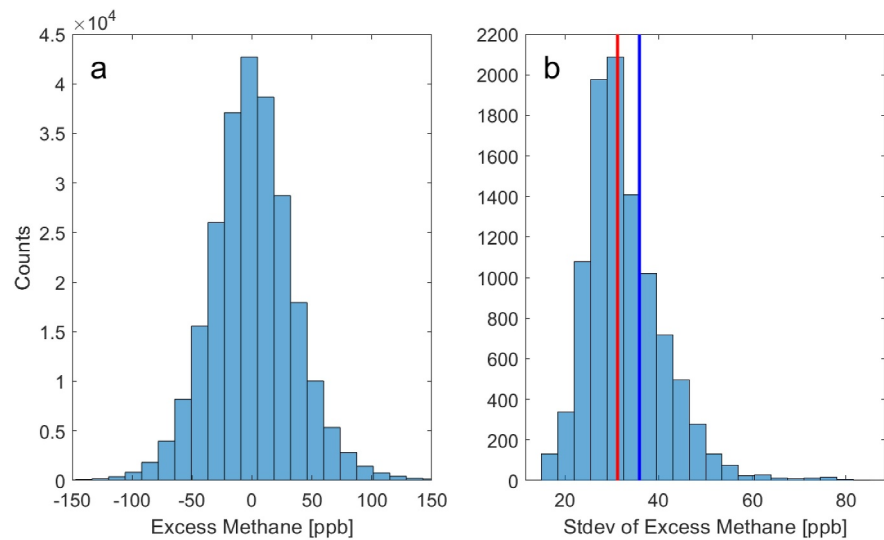


Figure 4. (a) Distribution of excess methane across the scene from Figure 1b; the standard deviation is 36 ppb (or 1.9% of the background); (b) Distribution of standard deviation with the 2×2 km boxes. The median of this distribution is 31 ppb (1.6%), indicated by the red line. The blue line shows the standard deviation, 36 ppb, from panel (a), for comparison.

by GHGSat. Terrain height was obtained from NOAA (2020). It could be argued that $\sqrt{\lambda}$ should be used instead of λ in Equation 3, for example, if the signal is shot-noise limited. However, this was found to produce a comparable fit and in the end the λ -dependence was retained.

Albedo was obtained from Moderate Resolution Imaging Spectrometer (MODIS), using multi-year averages of the MCD43C3 product (Schaaf et al., 2002), band 6. North American maps for snow-free and snow-covered conditions are shown in Figures B2 and B3.

Fits were performed considering data from C1 and C2–C5 separately. The latter were grouped together as there are fewer observations from them individually, are of the same (or very similar) design, and their calculated precision appears to be very similar. Results of these fits are given in Table 3. C1 was found to have a SZA-dependence with the best precision occurring for a SZA of about 60° ; C2–C5 showed little variation with SZA although the large majority of these data were for larger SZAs.

While variability of surface terrain was also found to be an important predictor of the precision, albedo was found to have the largest influence. There is good agreement between the fitted precision (from Equation 3) and the calculated precision as shown in Figure B1 in which the average \pm standard-deviation of the difference is $0 \pm 1\%$ and the coefficient of determination was 0.82, suggesting that this model captures much of the observed variability. See Appendix B for additional information.

Equation 3 was then used to estimate the expected methane precision from the C2 instrument across North America. Figure B4 shows this for snow-free conditions using the albedo map from Figure B2. In the central plains values are 1.5%, approaching 1% over the brightest surfaces, and with precisions around 2% being the most common.

3.2. Plume Modeling Using MLDPn

The MLDPn (Modèle Lagrangien de dispersion de particules d'ordre n) dispersion model (D'Amours et al., 2015; Hoffman et al., 2020) was used here to simulate methane plumes in order to quantify a detection limit and evaluate uncertainties (used in Section 4.2). MLDPn, the operational model used at ECCC to respond to environmental emergencies involving air contaminants, is a Lagrangian particle dispersion model. It uses meteorology from the North

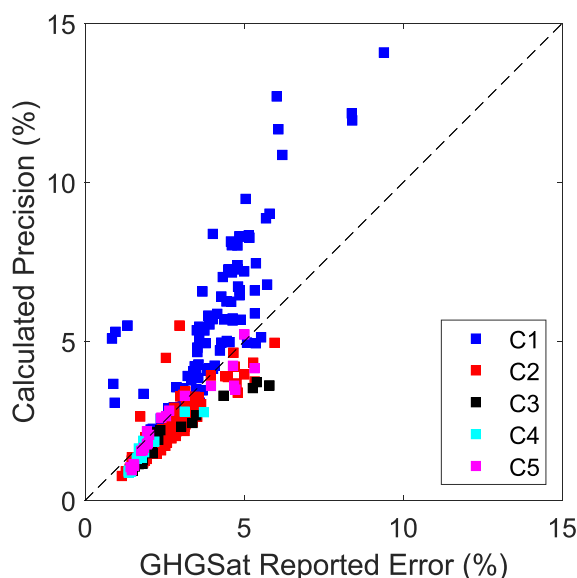


Figure 5. Comparison of the scene precision as calculated in this work with the GHGSat-reported uncertainty, averaged over each scene.

Table 3

Excess Methane Fit Parameters for Equation 3 and Typical Methane Precision Considering All 1,600 Sources Reporting to the Canadian GHG-RP Database for Three Scenarios (Snow Covered/Dark Surface: $\lambda = 0.1$, $\theta_0 = 60^\circ$, Average Albedo: $\lambda = 0.2$, $\theta_0 = 30^\circ$, Bright Surface: $\lambda = 0.35$, $\theta_0 = 30^\circ$)

Satellite	a_1	a_2	a_3	a_4	a_5 (km ⁻¹)	Precision (%)		
						Snow	Average	Bright
C1	-3.35	2.41	8.38	-11.45	24.45	5.5	5.4	3.6
C2-C5	2.09	0.19	0.34	-4.15	9.24	2.6	2.1	1.5

America regional version of the Canadian operational weather forecast model GEM, or Global Environmental Multiscale model (Côté, Desmarais, et al., 1998; Côté, Gravel, et al., 1998; Girard et al., 2014). The meteorology used here are from forecasts launched at 12:00 UTC on a 2.5 km grid.

MLDPn was run at 100 m resolution for a prescribed source radius, varying from 10 m for a oil/gas well to 200 m for a larger landfill, emitted at a prescribed constant rate using GEM meteorology for the day, time, and location of the GHGSat scene. The resultant plume was interpolated onto a 25 m grid, the approximate resolution of GHGSat, and then a random, normally distributed noise was added to each pixel. The standard deviation of the noise was taken to be either the value obtained for that scene (as discussed in Section 3.1) or from a range of values chosen for the detection limit studies.

Figure 6 shows the comparison between the methane plume observed by GHGSat on 6 June 2021 and the MLDPn-modeled plume for that same time and location. The MLDPn plume was isolated from the background field by using the same number of pixels as the GHGSat plume, 198 in this case, and then normally distributed random error with a standard deviation of 1.1% (20 ppbv, calculated for this scene) was added. The MLDPn cannot match the detailed structure of the actual plumes, but nevertheless captures the overall size, aspect ratio, and variability. It is worth noting that a precision of 1.1% as used here was the best of the 249 scenes, and is a result of the higher albedo (0.34) and uniform terrain of this location.

3.3. Alternative Emission Algorithm

An alternative emission algorithm was applied to plumes in an effort to assess consistency with the GHGSat-IME method. This alternate approach is similar to the GHGSat-IME in that it employs a variant of the IME concept, but differs in several key regards.

The first key difference is that instead of a mask, the plume was isolated by fitting a 2D plane to the pixels within a specified box, where the plane is derived by only considering pixels below the median value. Only a fraction of the pixels within the box are expected to be enhanced by the plume and so using values below the median ensures avoiding the plume while keeping sufficient pixels for a reliable fit. Purely to facilitate the analysis, the plume was rotated about the source location (as provided by GHGSat) according to the wind direction so that the plume is aligned with the y-axis and converted into a relative distance from the source location (see, e.g., Pommier et al. (2013)). Thus, the location of each pixel is now expressed as an up/downwind and crosswind distance from the source. Once the background was removed the mass of the methane within the box was calculated as a function of downwind distance.

The second key difference lay in the wind speed. Instead of an effective wind speed, wind speed at a particular height, U_z , was used. MLDPn plume modeling indicates that, typically, half the plume mass resides below a height of 5 m and so this is the height that was used.

To more explicitly connect this alternative approach to the Varon et al. (2018) formulation in Equation 1, it can be expressed as:

$$Q' = \frac{U_z}{l} \sum_{j=1}^M (\Delta\Omega_j - \Delta\Omega_{bg,j}) \cdot A_j \quad (4)$$

Comparing Equations 4 and 1 reveals the summation is now over the M pixels in the box, l is the downwind length of the box, and a background excess methane, $\Delta\Omega_{bg,j}$ is subtracted. The ratio l/U_z can be interpreted as the time for the plume to traverse the box, similar to previous approaches (Adams et al., 2019).

4. GHGSat Evaluation

4.1. Wind Speed Comparisons

Knowledge of the wind speed is critical to obtaining accurate emission estimates and its uncertainty is often the single largest contributor to the emissions error budget (He et al., 2024; Varon et al., 2018). Here, variability

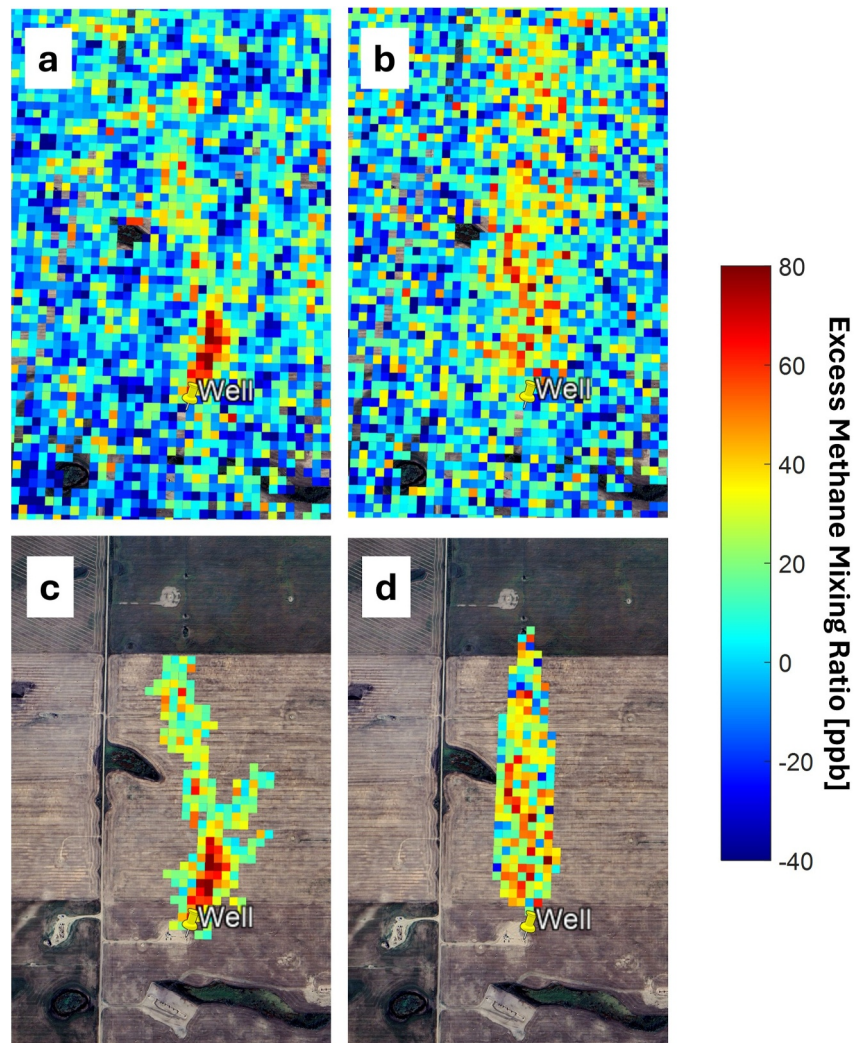


Figure 6. Excess methane for a scene from 6 June 2021, 17:25 UTC near Kindersley, Saskatchewan (51.61°N, 109.09°W). (a) GHGSat data, (b) MLDPn simulated methane field, using Global Environmental Multiscale model (GEM) meteorology at the time and location of the observed plume, assuming a methane precision of 1.2% and the GHGSat-derived emission rate of 468 kg/hr, (c) GHGSat showing only isolated plume, and (d) MLDPn isolated plume using the same number of pixels as the GHGSat isolated plume. GEM Winds are out of the south (179°) at 4.9 m/s.

among different sources of 10 m wind speed were used to estimate its uncertainty. These sources are GEOS-FP (Akraoui et al., 2023; Molod et al., 2012), ECMWF ERA-5 (Dee et al., 2011), MERRA-2 (Gelaro et al., 2017), and GEM (see Section 3.2). Note that GOES-FP (global forecast), and ERA-5 and MERRA-2 (global reanalyses) are at relatively coarse spatial resolutions. GHGSat provides its own GEOS-FP wind speed for scenes in which a plume was identified, but data were also downloaded from the NASA archive directly for all scenes.

A comparison of these various 10 m wind sources, using ERA5 as the reference, is shown in Figure 7. Each was interpolated in space and time to that of GHGSat scenes. Figure 7a shows the comparison for scenes with plumes. In the Varon et al. (2018) work, GEOS-FP winds are extrapolated from 50 m down to 10 m but it is unclear if this is done operationally. Comparing GEOS-FP winds from the original NASA files with the GHGSat reported values shows fairly modest differences, 0.23 ± 0.32 m/s, indicating that perhaps the 10 m winds were not extrapolated or that extrapolation did not introduce significant errors. The standard deviation of differences between the various data sets varied from 0.7 to 1.6 m/s.

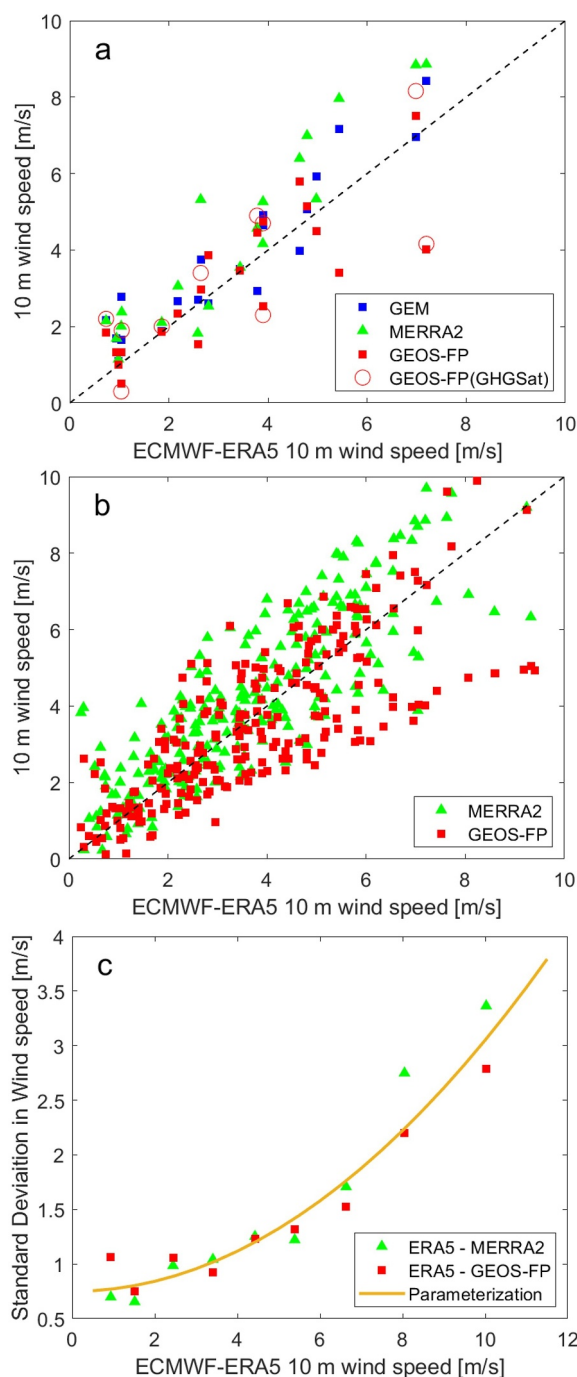


Figure 7. Comparison of 10 m wind speeds at GHGSat scene locations: (a) ECMWF ERA5 with Global Environmental Multiscale model, GEOS-FP, MERRA, and (possibly extrapolated) GEOS-FP from the GHGSat data files for days with identified plumes; (b) ECMWF ERA5 with GEOS-FP and MERRA2 for all 249 scenes; (c) Standard deviation between ERA5 and the other two sources a function of ERA5 wind speed. Equation 5, the fit to these data, is also plotted here.

A comparison of winds for all scenes is shown in Figure 7b. There is a reasonable agreement with standard deviations of 1.19, 1.28, and 1.37 m/s between pairs of the three wind sources. Varon et al. (2018) found a standard deviation of 1.6 m/s in comparisons of GEOS-FP 10 m wind with measurements from US airports.

It is clear upon inspection of Figure 7b that the variability among the different winds increases with wind speed. In an attempt to quantify this effect, standard deviation was calculated as a function of ERA5 wind speed and is

shown in Figure 7c. A function of the form $a + b \cdot u_{10}$ was not able to adequately account for the observed curvature, and so the absolute standard deviation, σ_{wind} (m/s), was represented by,

$$\sigma_{\text{wind}} = d_1 + d_2 \cdot U_{10}^2 \quad (5)$$

with $d_1 = 0.75$ and $d_2 = 0.023$, and for $U_{10} < 10$ m/s. This means uncertainty in wind speed is no smaller than 0.75 m/s. Equation 5 can be used as a measure of the random error in the wind speed. It is worth noting that the relative error, $\sigma_{\text{wind}}/U_{10}$, rises sharply below 3 m/s, to values of 1 or larger at the smallest wind speeds, but is largely flat at 0.25–0.30 for 3 m/s and above.

4.2. GHGSat Emission Detection Limit

Detection limit, alternatively referred to minimum detection limit, detection threshold, or limit of detection, is defined here as the minimum emission that leads to a detectable enhancement in methane above the background to within a stated confidence level and for a single scene (or overpass). Thus the detection limit, Q_{min} , is linked to the precision of the measurement system, σ_M ,

$$Q_{\text{min}} \propto q \cdot \sigma_M \quad (6)$$

where q represents standard score (z is reserved for a height-related quantity) for the desired confidence level, in number of standard deviations (e.g., $q = 1, 2, 3$ would correspond to confidence levels of 68.2%, 95.4%, and 99.7%, respectively), and σ_M is the a measure of the methane precision.

Equation 6 follows the general approach of other studies defining detection limit for methane emissions; however, there does not appear to be a consensus confidence level. For example, Dubey et al. (2023) opted to use $q = 3.3$ whereas Jacob et al. (2016) used $q = 2$ for detection limit and a more stringent $q = 5$ for an analogous quantification limit. In this work we adopt a $q = 2$ definition, and also point out that this can be readily scaled to another confidence level by applying a factor of $q'/2$, where q' is the standard score for the new confidence level.

These previous studies took σ_M as the precision of the methane itself, which is certainly a critical factor in a determination of detection limit. However, it is proposed here that a better quantity is the precision of the methane emissions which would combine the precision of the methane with any random errors introduced by the emissions retrieval algorithm.

To accomplish this, synthetic GHGSat plumes, simulated using the MLDPn model as described in Section 3.2, were used. MLDPn plumes were generated for each of the 14 scenes (at that time and location) in which a plume was found or assessed as a maybe. Normally distributed noise was added to the 25 m methane field with standard deviations from 0% to 5%. Likewise, input emissions were varied from 0 to 1,000 kg/hr. Each combination of methane precision and emissions was repeated 50 times for each scene in order to build up sufficient statistics.

An emission rate from each simulated plume was then determined using an emissions algorithm that mimics, to the extent possible, that used by GHGSat. Since the goal here is to estimate the detection limit for GHGSat using their existing processing approach, it is important to capture the essence of their method. Note that this is in contrast to Section 4.3 which aims to compare reported emissions using an alternative emissions retrieval approach, formulated using different assumptions, in order to better understand how different algorithms might lead to different emissions.

For a given scene, a plume is defined as being composed of the same number of pixels as the GHGSat-identified plume. Moreover, as we do not know the precise nature of their plume masking, we were unable to implement it anyway. In parallel with Varon et al. (2018), a $U_{\text{eff}} = f(U_{10})$ relationship was derived for these synthetic data to remove systematic biases. Here $U_{\text{eff}} = 0.75 \cdot U_{10}$ was the relationship obtained.

The results are shown in Figure 8. Figure 8a shows a box-plot of the retrieved emissions across all 14 locations for a methane precision of 2%. There was no bias, a result of defining U_{eff} as mentioned above. The variability was found to increase with input emissions. The overall correlation between individual retrieved and input emissions was 0.92. The variability of the difference between the retrieved and true emissions represents the precision of the retrieved methane emissions (σ_M), a combination of the random uncertainty from the retrieval method combined

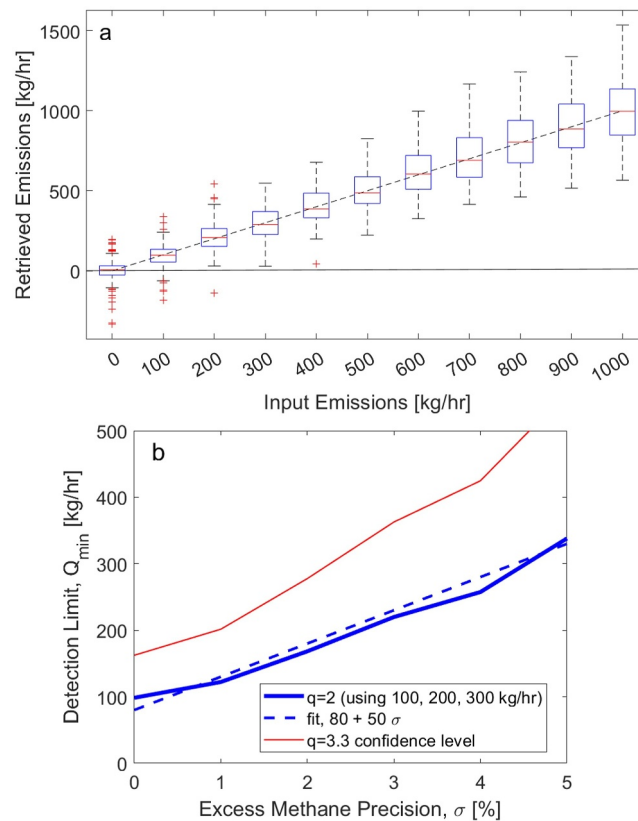


Figure 8. Summary of GHGSat detection limit model study: (a) box plot of retrieved emissions across 14 locations as a function of input (specified) emissions for a methane precision of 2%. The red lines represent median, and the blue box denotes the 25–75th percentiles, the black bars the 10th–90th percentiles, and the red pluses are the outliers. (b) The GHGSat detection limit as a function of methane precision considering input emission values of 100–300 kg/hr and a confidence level for $q = 2$. Also shown is the linear fit to these data, the corresponding value for a confidence level for $q = 3.3$.

with methane precision. It is noted that even for perfect data (a methane precision of 0), there are still random errors in the retrieved emissions.

From this, the detection limit was determined by considering only true emissions values comparable with its expected range. Hence, the variability of emissions for input emissions of 100, 200, and 300 kg/hr were combined. Considering these together, the emissions variability, (or precision) was found to increase linearly with the methane precision, approximately as $\sigma_M = 40 + 25 \cdot \sigma$. The resultant detection limit, using Equation 6 for $q = 2$, is shown in Figure 8b as a function of methane precision. As the random errors get larger the detection limit deteriorates. Also, the non-zero detection limit for noise-free methane data points to the (effective) random error of the retrieval algorithm itself. It arises from the fact that the $U_{\text{eff}} = 0.75 \cdot U_{10}$ relationship is only a best fit and the true relationship varies with location and time. This result supports our decision to include the random errors introduced by the retrieval method as simply considering methane precision would suggest a perfect emissions retrieval is possible.

The $q = 2$ detection limit from Figure 8b can be approximated as,

$$Q_{\min} = 80 + 50 \cdot \sigma \quad (7)$$

where σ is in percent. Thus a precision of 1% provides a detection limit of 130 kg/hr, as might be the case for C2–C5 under the most favorable conditions, and a precision of 5% would result in 330 kg/hr, reasonable for C1 under fairly typical conditions. For comparison, Figure 8b also shows the $q = 3.3$ detection limit which is consistent with the definition used by Dubey et al. (2023).

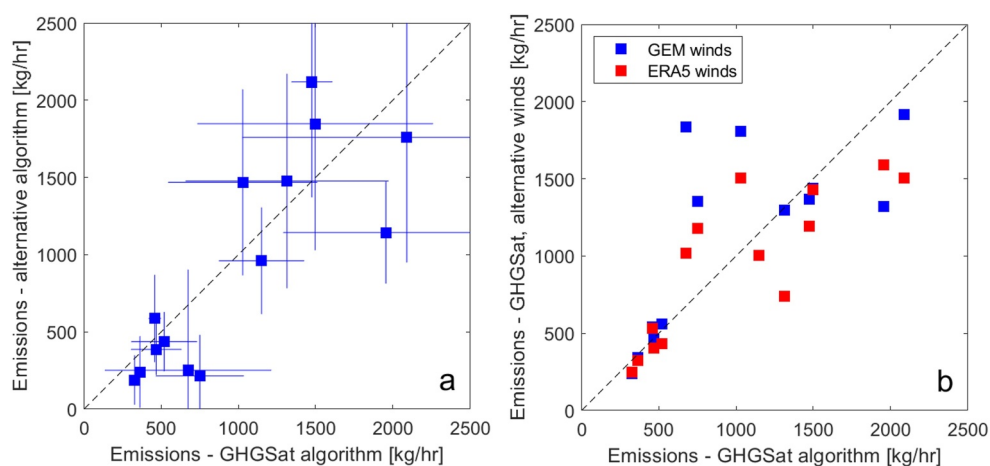


Figure 9. (a) Comparison of GHGSat-derived emissions and uncertainties with those using the alternative integrated mass (or methane) enhancement algorithm. (b) Comparison of GHGSat emissions with the same GHGSat emissions but using another source of wind speed data.

Assuming this relationship holds for locations and times not explicitly modeled here, the detection limit for C2–C5 across North America can be estimated using Equation 7 combined with precisions from Figure B4. This is shown in Figure B5. The central plains show values of 120–150 kg/hr with much of Canada and the eastern US roughly at 180 kg/hr. Due to much more variability in terrain height, the detection limit is more like 300+ kg/hr in Western North America.

4.3. Emissions Comparison

Emissions were calculated using the alternative approach outlined in Section 3.3 for the 14 scenes with plumes. Initially, the GHGSat-provided 10 m wind speeds, mapped to a height of 5 m using the ERA5 wind profile shape, were used in order to remove (or minimize) the source of the wind speed as a source of difference. Figure 9a shows the comparison. There is a reasonable correspondence between the two, with a correlation (0.82), the GHGSat emissions slightly larger, 70 kg/hr, on average, and the with error bars intersecting the 1:1 line for most of the plumes. The larger differences tend to coincide with the plumes that visually appear to be less distinct, suggesting a greater sensitivity to how the plumes are defined or isolated from the background. Maps of all plumes are provided in the data archive (Environment and Climate Change Canada, 2023a). Uncertainties are discussed below. This general consistency suggests that the different approaches taken by the two methods (plume masking vs. background removal and use of an effective wind speed vs. an actual wind speed with a height chosen using modeling) did not lead to any significant inconsistencies in the emissions. Of course no insight can be gained as to their accuracies as there is no truth or reference to compare with.

Considering now the effect of wind speed on emissions, Emissions using the GHGSat-algorithm were recalculated using different sources of U_{10} in the expression for U_{eff} . Equation 2. Figure 9b shows this comparison for emissions using GEM and ERA-5 winds. For some scenes this can lead to difference of a factor of 2 or more and underscores its important on the magnitude of the emissions.

4.4. Emissions Uncertainties

For many applications the uncertainty in the emission rate is arguably as important as the rate itself. There are different possible sources of uncertainty that might be considered, related to either the level 2 data, the emissions algorithm, or the external data used. Varon et al. (2018) considered two sources of random errors when quantifying the uncertainty of GHGSat emissions: the precision of the excess methane and wind speed.

Varon et al. (2018) found the methane precision contributed to an uncertainty in emissions of 70 kg/hr + 5% for 1% precision and 130 kg/hr + 7% for 3% (see their Table 1). Wind speed uncertainties were explored in Section 4.1. One interesting aspect of the Varon et al. (2018) IME approach is that emissions are proportional to an *effective* wind speed, which itself is a linear function of an actual (10 m) wind speed. Hence the uncertainty due to

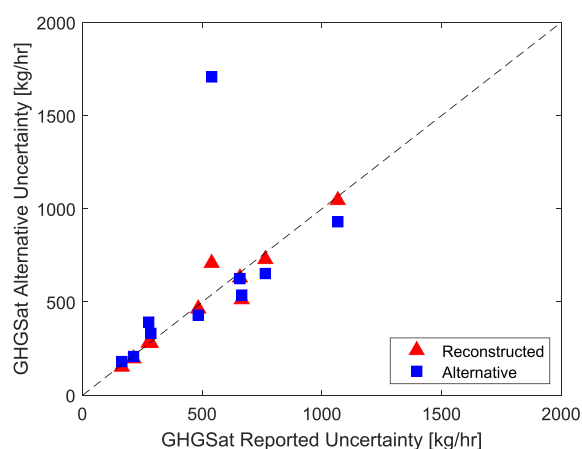


Figure 10. Comparison of GHGSat reported uncertainties with reconstructed and alternate uncertainties.

wind speed is damped, particularly at low wind speeds. The relative uncertainty in effective wind speed (and hence emissions) is proportional, not to $1/U_{10}$, but rather to $b_2/(b_1 + b_2 \cdot U_{10})$ according to Equation 1. This result can be found using error propagation by calculating $(\Delta Q/\Delta U_{10})/Q$ and combining equations Equations 1 and 2. Thus the maximum possible uncertainty is $b_2/b_1 = 0.35/0.40$ or about 0.88 (88%). In practice, this arises as the effective wind speed can never be smaller than $b_1 = 0.40$ m/s, even for perfectly calm conditions. Physically this does not seem reasonable and may simply be an artifact of the U_{eff} fit. Consider, for example, a wind speed of 0.3 m/s, as was the case in one GHGSat reported plume (see the last plume in Table A1). This would imply that emissions might be derived with an uncertainty as low as 69%.

Uncertainties for 10 of the plumes were provided by GHGSat, with relative values varying from 24% to 80% (see Table A1). How these were determined is not clear but it is assumed to be similar as that from Varon et al. (2018). In an attempt to reconstruct the GHGSat uncertainties, a 1% uncertainty in methane for C2–C5 and 3% for C1 was assumed (see Table 1 in Varon et al. (2018)). Additionally, a constant 1.5 m/s uncertainty in U_{10} was assumed, found through trial and error, and propagated through the $U_{\text{eff}} = f(U_{10})$ relationship. This led to the emissions uncertainty comparison in Figure 10, which shows excellent agreement between reconstructed and GHGSat uncertainties for 8 or the 10, and slightly larger differences for the latest two, chronologically speaking. The largest difference was for a wind speed of 0.3 m/s, but this still matched the reported uncertainties within 30%.

In addition to trying to understand how GHGSat uncertainties were derived, uncertainties consistent with the findings of this work were calculated. Scene specific methane precisions were used combined with the wind speed-dependent uncertainty (see Section 4.2). Instead of using the relative error in U_{eff} , the U_{10} wind speed-dependent uncertainty from Equation 5 was used. These are also shown in Figure 10 and, overall, are not that different from the GHGSat reported uncertainties. The only noteworthy exception is for the scene with a wind speed of 0.3 m/s where the calculated uncertainty is more than 3-times as large.

Despite some differences in the formulation of the uncertainties, the overall consistency between GHGSat-reported and those calculated here suggests these are not particularly significant. The only exception appears to be for low wind speeds. From the results here, a 10 m wind speed of 1 m/s has a 1-sigma uncertainty of 100%. The most straightforward way of reconciling this difference, and the one recommended here, is to not consider plumes with a wind speed below 1 m/s.

Detection limit is generally considered to be a property of the instrument, which is governed by spatial resolution and methane precision. However, in practice environmental factors influence the detectability of a plume. One example is the reflectivity of the scene, which is already folded into the detection limit via the scene precision. Another is wind speed, which is not accounted for thus far. For example, a 200 kg/hr emission may be above the detection limit for a wind speed of 4 m/s, but may also be below the detection limit for a wind speed of 8 m/s. The faster winds lead to a more rapid dispersion of the plume, smaller per-pixel methane enhancements, which are more likely to be near or below the noise level. This nuance was explored by re-examining the synthetic plume data set created for the detection limit study.

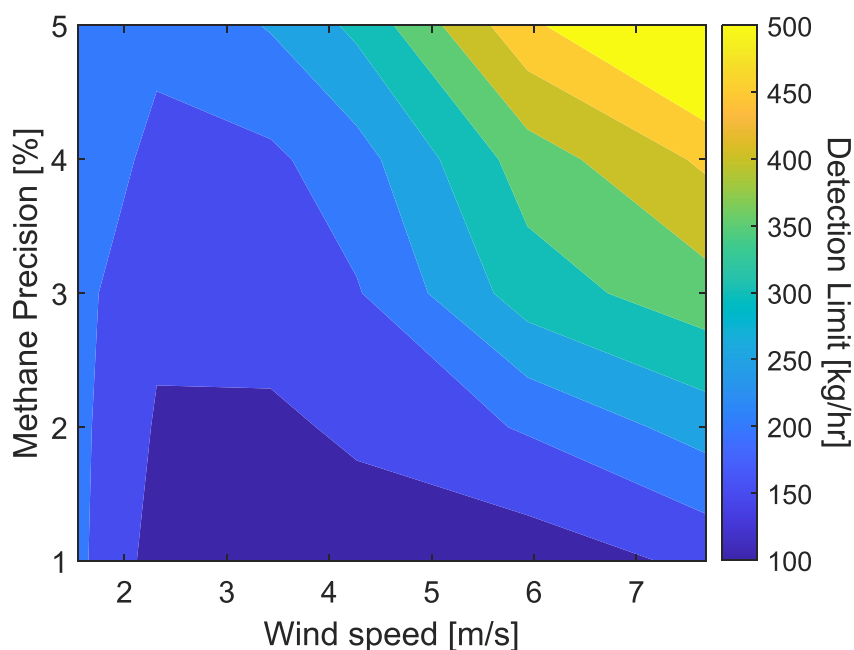


Figure 11. A GHGSat “environmental” detection limit (which includes the uncertainty of the wind speed) as a function of methane precision and wind speed.

Using the same $q = 2$ confidence level, detection limit was re-calculated as a function of wind speed. The emission precision results of Section 4.2 are used as a starting point and added to this, in quadrature, was the uncertainty of the wind speed from Figure 7c. This culminated in Figure 11 which shows an “environmental” detection limit as a function of precision and wind speed. The best detection limits are found for wind speeds between 3 and 5 m/s (roughly, 110 kg/hr for 1% precision) and increasingly deteriorate for winds outside of this range. The detection limit at low wind speeds (<2 m/s) is governed by the uncertainty in the wind speed themselves, whereas for fast winds (>5 m/s) it is the reduced signal-to-noise from the increased dispersion effect.

4.5. Link to Plume Detection Rate

As stated above, the choice of scene location was a combination of locations requested by ECCC and those chosen by GHGSat using their machine learning algorithm that examines data from multiple satellite instruments to decide what locations are most promising. It is estimated that the breakdown is as follows: one-third requested by ECCC for oil and gas locations of interest in Western Canada, one-third requested by ECCC chosen from the top-emitters across different sectors in the Canadian 2020 GHG-RP database, and one-third chosen by GHGSat.

The 245 scenes over 133 distinct locations yielded 10 plumes (6 confirmed, 4 maybe), where the 4 hand-picked scenes with plumes are omitted from this analysis, resulting in a detection rate of $10/245 = 4.1\%$, or $6/245 = 2.5\%$ if one argues the maybes should also be omitted. Clearly, for the large majority of scenes, methane emissions, if any, were below the GHGSat detection limit. But was this due simply to modest emissions at a site, or more substantial, but intermittent, emissions that they were usually missed? For the oil and gas sector, there were only 2 detections (1 confirmed, 1 maybe) from 145 scenes. Here, at least, based on distributions of emissions from oil and has obtained from recent aircraft surveys over Western Canada, it appears that only a tiny fraction of sources would typically be detectable (Conrad et al., 2023; Johnson et al., 2023b). More study is required to understand the implications of this given the heavy-tail nature that is more typical of these distributions (Frankenberg et al., 2016) (i.e., that relatively few sites emit a substantial fraction of total emissions).

To further shed some light on this issue, GHG-RP emissions were linked to the GHGSat data by finding the largest reported annual emission rate within each scene and converting it to an hourly rate. Of the 245 scenes, 135 had non-zero values. From these 135 scenes, 47 locations, according to GHG-RP, emitted methane at rate above the detection limit specific to that scene (including snow/no-snow) and GHGSat instrument (see Section 4.2). Therefore if emissions were constant throughout the year one would expect GHGSat to typically identify a plume.

Of these 47, 6 scenes contained a detected GHGSat emission (3 confirmed, 3 maybe), all for the landfills (waste sector). Within this 47, only 10 were oil and gas scenes, which is qualitatively consistent with the aircraft surveys which suggest that not many detections should be expected. In fact the only GHGSat oil and gas detections were for scenes where GHG-RP indicated virtually no emissions.

Switching to the waste sector, it is interesting that of these 6 scenes containing plumes, the GHG-RP emissions were 4–10 times (6.6 times on average) larger than their individual detection limits. Considering the other side, there were 5 other landfill scenes without GHGSat detections where the GHG-RP emissions–detection limit ratio was in this same range. The overall detection rate for landfills, 8 (5 confirmed + 3 maybes) out of 79, was much more favorable at 10% with an even higher detection rate, $6/32 = 19\%$ when the detection limit exceeded the GHG-RP emissions.

Clearly these are preliminary findings; a more comprehensive evaluation of this topic is reserved for a follow-up study. If nothing else this highlights the challenge in maximizing plume detections for target-based remote sensing systems.

5. Summary

An independent evaluation of methane emissions using data from GHGSat satellites C1–C5 was conducted. Each GHGSat platform is a 15 kg microsatellite flying a Fabry-Perot short wave infrared spectrometer. There are currently 11 methane-sensitive satellites in the constellation. The design of C2–C5 are the same, with C1 lacking some additional order filtering. The GHGSat data used here consisted of excess methane, reflectivity, errors and quality flag, and, where detected, plume and emissions information from 249 scenes were analyzed. From these, 10 scenes contained confirmed methane plumes, with four of these 10 provided by GHGSat to augment the number of plumes to be analyzed.

Excess methane precision was calculated for each scene by analyzing the standard deviation of excess methane in $2 \times 2 \text{ km}^2$ blocks of pixels based on the assumption that the vast majority of observed variability is from random error from the instrument or retrieval. Precision values of 5%/2% were found to be typical for the C1/C2–C5 satellites, with some variability due to scene albedo and other factors. The precision of scenes from C2–C5 occasionally reached 1%, but this was for more reflective and uniform terrain locations. Scene.

Modeling with a Lagrangian plume dispersion model indicates typical detection limits of 240/180 kg/hr (C1/C2–C5), with a best case of roughly 100 kg/hr. Emissions and their uncertainties calculated using an alternative approach were found to be in broad agreement with GHGSat-reported values. Overall, the performance of the C2 design (also used for C3 onward) was found to be generally consistent with that put forth by GHGSat.

The plume detection rate was 10 out of 245 overall, and 2 (or 1 if only confirmed plumes are counted) out of 145 for the oil and gas sector, likely a result of the large majority of sources emitting below the detection limit. The most plumes were found over landfills which had a more promising detection rate of 10% overall, or 19% if limited to scenes where the detection limit exceeded the GHG-RP emission rate.

Finally, based on the findings of this study, the following suggestions are made to GHGSat as to how they might improve their service. It is noted here that some of these rely on assumptions that may not be entirely correct.

1. Winds: (a) Emissions for wind speed below some threshold not be reported. A value of no more than 1 m/s is suggested here. (b) To use a source of 10 m wind speed directly and avoid using extrapolation as in Varon et al. (2018) (if indeed this is being done). (c) To use more than one source of 10 m wind speed forecast or reanalysis data, and using the mean value for the determination of emission rate. For example, using a second source from the ECMWF family of products.
2. If a plume is screened as maybe, provide information as to what factor(s) prevented it from being a confirmed plume; individual operators may have site specific knowledge that could help with this,
3. For scenes in which a plume was not detected, provide a scene-specific detection limit, and hence an estimate of the upper limit to what any single point source in that scene could be emitting.
4. Assuming this is not being done already, consider expanding the error budget to include the impact of the emissions algorithm itself. This could be the alternate flux method also detailed in Varon et al. (2018) or something else. This second algorithm could be run on a selection of representative scenes to establish

statistics, or on each scene operationally with the difference in emissions used as an additional term in the uncertainty budget.

Appendix A: Plume Data

Data layer images for a scene observed by C1 is given in Figure A1 for a landfill in Manitoba, Canada. No plume was detected in this image. Images such as these, and the original GHGSat data, for all 249 scenes are available from Environment and Climate Change Canada (2023a).

Information on the 14 scenes containing plumes that were used in this study is given in Table A1. A more detailed summary of all 249 plumes is also available (Environment and Climate Change Canada, 2023a).

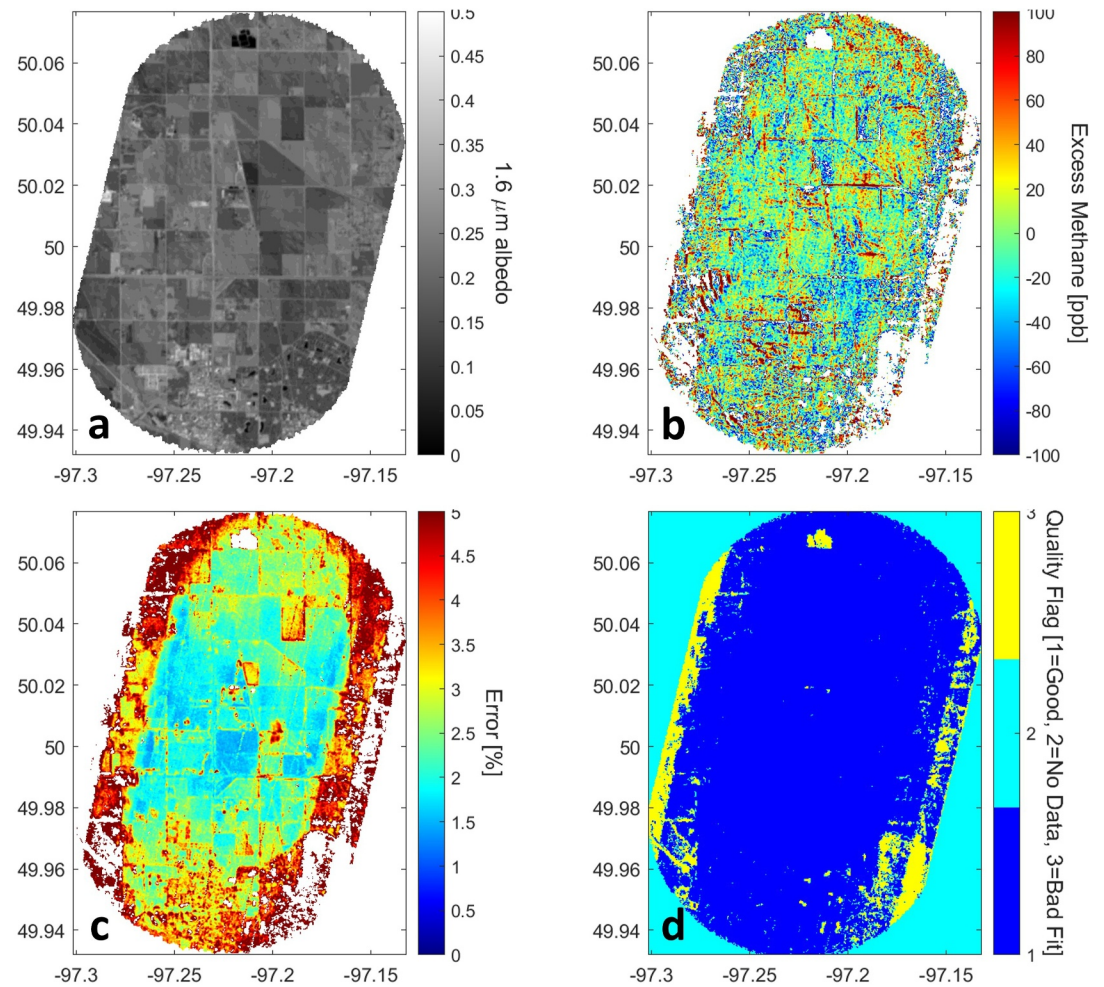


Figure A1. Data layers for a scene over the Prairie-Green Landfill, taken on 07 November 2021, 15:23 UTC (10:54 LST) from GHGSat-C1: (a) the 1.6 μm reflectivity, (b) Excess methane, (c) Reported error of the excess methane, and (d) quality flag. No plume was identified. Calculate precision was 3.4%.

Table A1
Summary of 14 GHGSat Observed Plumes

Name	Type	Satellite	Date	UTC	Calculated precision (%)	Source location	Wind speed (m/s)		Emissions (kg/hr)	Note
							GEOS-FP	GEM		
Kindersley	Well	C2	2021-06-13	17:25	1.16	51.61, -109.09	4.7	4.6	468 ± 35%	1
Kindersley	Well	C2	2021-06-22	17:25	1.33	51.61, -109.09	3.4	3.8	519 ± 41%	1
Lachenaie	Waste	C2	2021-07-24	14:56	1.93	45.75, -73.54	2.0	1.9	1,497 ± 51%	1
Essex Windsor	Waste	C1	2021-08-22	16:25	5.55	42.09, -82.87	2.2	2.6	1,315 ± 50%	1
Essex Windsor	Waste	C1	2021-09-10	16:21	3.81	42.08, -82.86	(3.0)	2.7	1,476 ± (35%)	2
Keele Valley	Waste	C1	2021-09-11	16:06	2.99	43.87, -79.50	8.2	7.0	1,150 ± 24%	
Brady Road	Waste	C1	2021-10-07	17:23	3.68	49.73, -97.20	4.2	8.4	750 ± 38%	
Beaver Regional	Waste	C2	2021-11-02	17:28	1.58	53.30, -112.39	(4.0)	2.6	328 ± (36%)	2
Essex	Waste	C2	2021-12-10	15:23	1.73	42.09, -82.87	1.9	1.6	2,091 ± 51%	
Lloydminster	Well	C2	2022-01-19	17:32	2.50	53.30, -109.68	(2.8)	3.5	458 ± (41%)	2
Sudbury Landfill	Waste	C2	2022-01-31	17:21	2.15	46.5, -80.9	(1.2)	1.1	362 ± (86%)	2
Brady Road	Waste	C2	2022-02-02	16:33	1.98	49.76, -97.19	2.3	4.9	1,028 ± 47%	
Twin Creeks	Waste	C2	2022-02-08	15:28	1.27	42.97, -81.87	4.9	2.9	1,955 ± 34%	
Duvernay	Waste	C3	2022-11-12	21:37	3.44	53.71, -117.27	0.3	2.8	674 ± 80%	

Note. 1 = additional plumes provided by GHGSat to augment database and 2 = plume identified as maybe. Values in brackets are reconstructed from the overall data set and not provided by GHGSat.

Appendix B: North American Maps

Fitted coefficients for Equation 3 were derived using a linear regression considering scenes from C1 and then C2–C5. For C1 the root-mean-square difference between the fitted precision and the calculated values was 1.6% with a coefficient of determination (R^2) of 0.69. For C2–C5, these were 0.67% with $R^2 = 0.65$. The scatterplot is shown in Figure B1. Combining all scenes (C1–C5) these were 1.0% and $R^2 = 0.82$.

The fitting above used average MODIS 1.6 μm snow-free and snow albedo, shown in Figures B2 and B3, respectively. As the chosen parameterization was able to capture most of the variability in scene precision it was

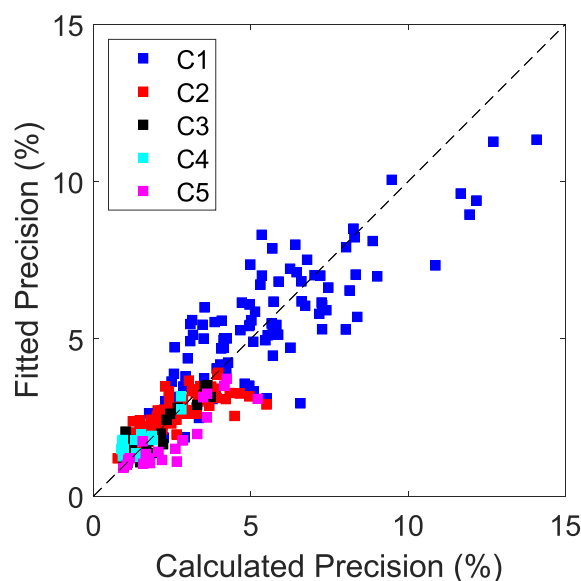


Figure B1. Comparison of estimated precision, based on scene albedo, terrain roughness, and solar zenith angle via Equation 3 with the calculated precision.

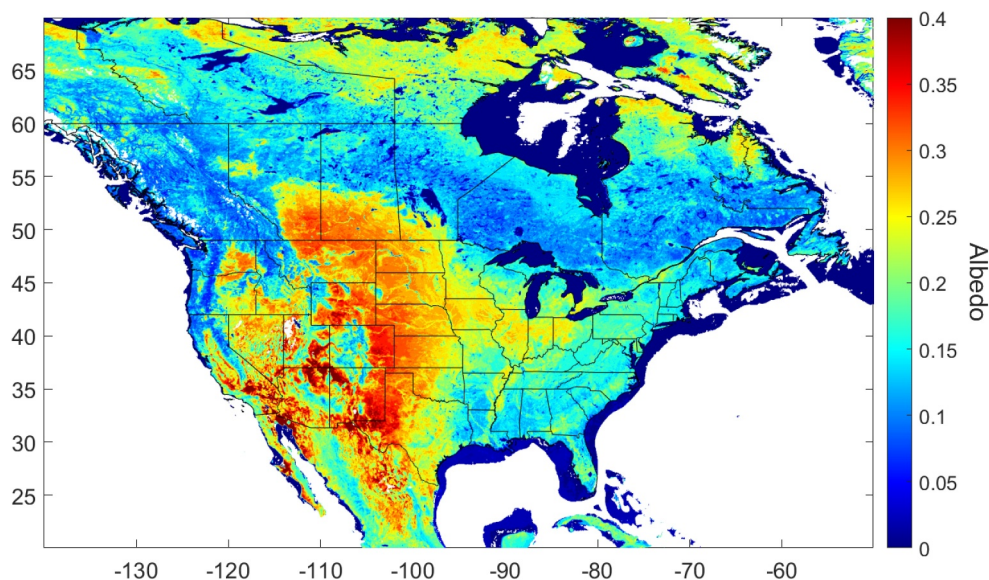


Figure B2. Mean MODIS MCD43C3 band 6 (1.64 μm) snow-free albedo, averaged using 2018–2021, April–October, snow = 0.

considered suitable to estimate GHGSat methane precision at all locations across North America. C2–C5 precision is shown in Figure B4 for snow-free conditions, using albedo from Figure B2.

The North America wide (snow-free) detection limit for C2–C5 can also be estimated by utilizing the precisions from Figure B4 together with Equation 7. These are shown in Figure B5.

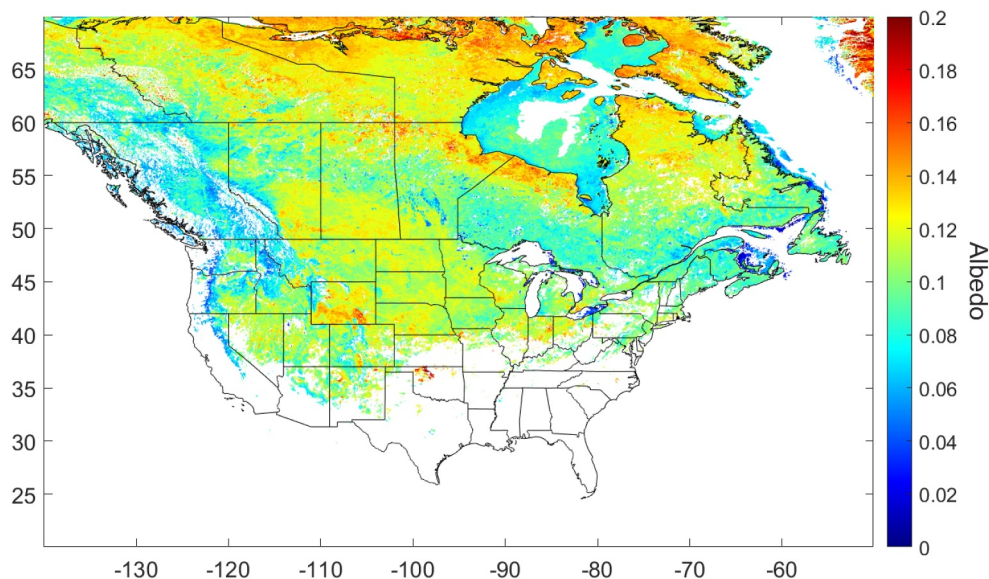


Figure B3. Mean MODIS MCD43C3 band 6 (1.64 μm) snow albedo, averaged using 2018–2021, November–March, snow = 100.

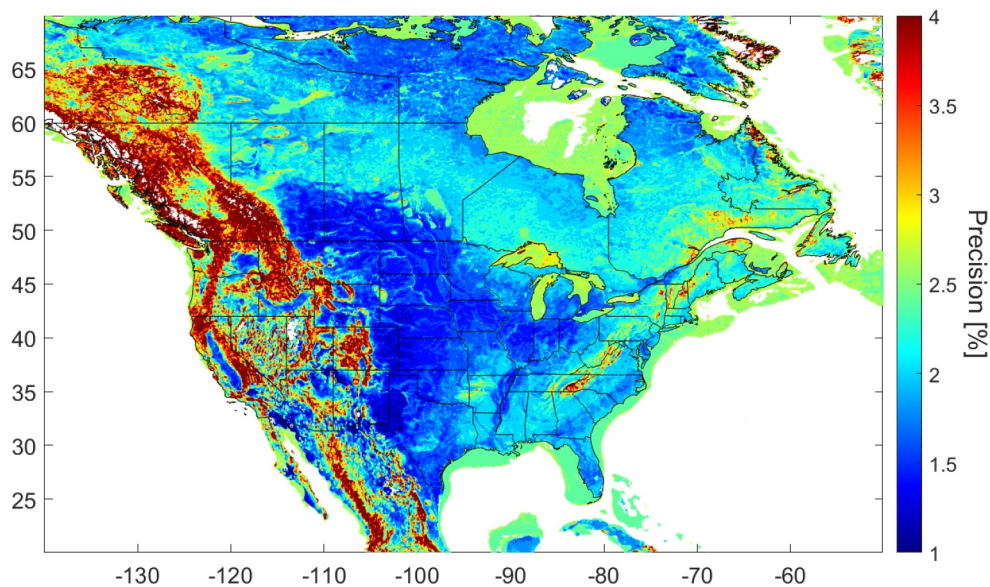


Figure B4. GHGSat-C2–C5 methane precision for snow-free conditions, calculated using Equation 3 and albedo from Figure B2.

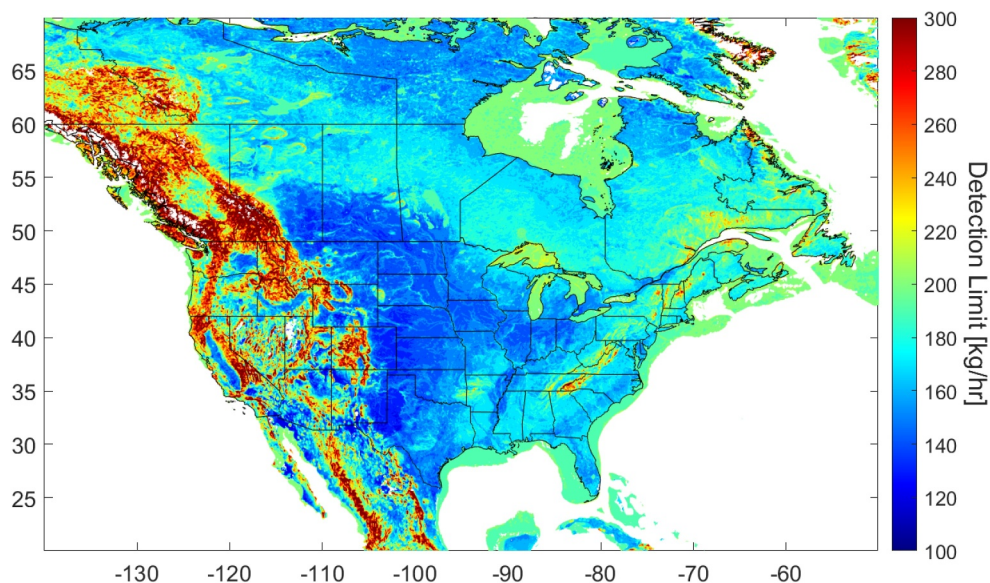


Figure B5. GHGSat-C2–C5 detection limit for snow-free conditions, calculated using Equation 7 and C2–C5 precision from Figure B4.

Data Availability Statement

The GHGSat data used here, with linked meteorological information is, are free to use and openly available from the ECCC collaboration site (Environment and Climate Change Canada, 2023a). The use of this data is subject to the Open Government License—Canada (Government of Canada, 2024). Also available are images for each scene analogous to those in Figures 1 and A1. Meteorological data were obtained as follows: ERA5 from ECMWF (Hersbach & Coauthors, 2020); MERRA-2 (Global Modeling and Assimilation Office (GMAO), 2015) and GEOS-FP (NASA Global Modeling and Assimilation Office, 2023) data are from the NASA Global Modeling and Assimilation Office (managed by the Goddard Earth Sciences Data and Information Services Center). MODIS 1.6 μm MCD43C3 albedo data were downloaded from (Schaaf & Wang, 2015).

Acknowledgments

The GEOS data used in this study have been provided by the Global Modeling and Assimilation Office (GMAO) at NASA Goddard Space Flight Center through the online data portal in the NASA Center for Climate Simulation. The authors thank the GHGSat team for providing some additional technical information on their hardware and data processing. The authors acknowledge the provision of GHGSat scenes from a European Space Agency/Canadian Space Agency data opportunity.

References

Adams, C., McLinden, C., Shephard, M., Dickson, N., Dammers, E., Chen, J., et al. (2019). Satellite-derived emissions of carbon monoxide, ammonia, and nitrogen dioxide from the 2016 horse river wildfire in the fort McMurray area. *Atmospheric Chemistry and Physics*, 19(4), 2577–2599. <https://doi.org/10.5194/acp-19-2577-2019>

Akkraoui, A. E., Privé, N. C., Errico, R. M., & Todling, R. (2023). The GMAO hybrid 4d-EnVar observing system simulation experiment framework. *Monthly Weather Review*, 151(7), 1717–1734. <https://doi.org/10.1175/MWR-D-22-0254.1>

Atherton, E., Risk, D., Fougère, C., Lavoie, M., Marshall, A., Werring, J., et al. (2017). Mobile measurement of methane emissions from natural gas developments in northeastern British Columbia, Canada. *Atmospheric Chemistry and Physics*, 17(20), 12405–12420. <https://doi.org/10.5194/acp-17-12405-2017>

Baray, S., Darlington, A., Gordon, M., Hayden, K. L., Leithead, A., Li, S.-M., et al. (2018). Quantification of methane sources in the Athabasca Oil Sands Region of Alberta by aircraft mass balance. *Atmospheric Chemistry and Physics*, 18(10), 7361–7378. <https://doi.org/10.5194/acp-18-7361-2018>

Baray, S., Jacob, D. J., Maasackers, J. D., Sheng, J.-X., Sulprizio, M. P., Jones, D. B. A., et al. (2021). Estimating 2010–2015 anthropogenic and natural methane emissions in Canada using ECCS surface and GOSAT satellite observations. *Atmospheric Chemistry and Physics*, 21(23), 18101–18121. <https://doi.org/10.5194/acp-21-18101-2021>

Buchwitz, M., de Beek, R., Burrows, J. P., Bovensmann, H., Warneke, T., Notholt, J., et al. (2005). Atmospheric methane and carbon dioxide from SCIAMACHY satellite data: Initial comparison with chemistry and transport models. *Atmospheric Chemistry and Physics*, 5(4), 941–962. <https://doi.org/10.5194/acp-5-941-2005>

Chan, E., Worthy, D. E. J., Chan, D., Ishizawa, M., Moran, M. D., Delcloo, A., & Vogel, F. (2020). Eight-year estimates of methane emissions from oil and gas operations in western Canada are nearly twice those reported in inventories. *Environmental Science & Technology*, 54(23), 14899–14909. <https://doi.org/10.1021/acs.est.0c04117>

Conrad, B. M., Tyner, D. R., Li, H. Z., Xie, D., & Johnson, M. R. (2023). A measurement-based upstream oil and gas methane inventory for Alberta, Canada reveals higher emissions and different sources than official estimates. *Communications Earth & Environment*, 4(1), 416. <https://doi.org/10.1038/s43247-023-01081-0>

Côté, J., Desmarais, J., Gravel, S., Méthot, A., Patoine, A., Roch, M., & Staniforth, A. (1998). The operational CMC-MRB global environmental multiscale (GEM) model. Part ii: Results. *Monthly Weather Review*, 126(6), 1397–1418. [https://doi.org/10.1175/1520-0493\(1998\)126<1397:tocmge>2.0.co;2](https://doi.org/10.1175/1520-0493(1998)126<1397:tocmge>2.0.co;2)

Côté, J., Gravel, S., Méthot, A., Patoine, A., Roch, M., & Staniforth, A. (1998). The operational CMC-MRB global environmental multiscale (GEM) model. Part i: Design considerations and formulation. *Monthly Weather Review*, 126(6), 1373–1395. [https://doi.org/10.1175/1520-0493\(1998\)126<1373:tocmge>2.0.co;2](https://doi.org/10.1175/1520-0493(1998)126<1373:tocmge>2.0.co;2)

Cusworth, D. H., Jacob, D. J., Varon, D. J., Chan Miller, C., Liu, X., Chance, K., et al. (2019). Potential of next-generation imaging spectrometers to detect and quantify methane point sources from space. *Atmospheric Measurement Techniques*, 12(10), 5655–5668. <https://doi.org/10.5194/amt-12-5655-2019>

D'Amours, R., Malo, A., Flesch, T., Wilson, J., Gauthier, J.-P., & Servranckx, R. (2015). The Canadian meteorological centre's atmospheric transport and dispersion modelling suite. *Atmosphere-Ocean*, 53(2), 176–199. <https://doi.org/10.1080/07055900.2014.1000260>

Dee, D. P., Uppala, S. M., Simmons, A. J., Berrisford, P., Poli, P., Kobayashi, S., et al. (2011). The ERA-interim reanalysis: Configuration and performance of the data assimilation system. *Quarterly Journal of the Royal Meteorological Society*, 137(656), 553–597. <https://doi.org/10.1002/qj.828>

Dubey, L., Cooper, J., & Hawkes, A. (2023). Minimum detection limits of the TROPOMI satellite sensor across North America and their implications for measuring oil and gas methane emissions. *Science of the Total Environment*, 872, 162222. <https://doi.org/10.1016/j.scitotenv.2023.162222>

Environment and Climate Change Canada. (2022). Faster and further: Canada's methane strategy. Retrieved from <https://publications.gc.ca/site/eng/9.915545/publication.html>

Environment and Climate Change Canada. (2023a). Government of Canada collaboration data - GHGSat [Dataset]. Retrieved from <https://collaboration.cmc.ec.gc.ca/cmc/arqi/GHGSat>

Environment and Climate Change Canada. (2023b). Greenhouse gas reporting Program (GHGRP) [Dataset]. Retrieved from <https://open.canada.ca/data/en/dataset/a8ba14b7-7f23-462a-bdbb-83b0ef629823>

European Space Agency. (2023). GHGSat data. Retrieved from <https://earth.esa.int/eogateway/missions/ghgsat>

Festa-Bianchet, S. A., Tyner, D. R., Seymour, S. P., & Johnson, M. R. (2023). Methane venting at cold heavy oil production with sand (chops) facilities is significantly underreported and led by high-emitting wells with low or negative value. *Environmental Science & Technology*, 57(8), 3021–3030. <https://doi.org/10.1021/acs.est.2c06255>

Forster, P., Storelvmo, T., Armour, K., Collins, W., Dufresne, J.-L., Frame, D., et al. (2021). Chapter 7: The earth's energy budget, climate feedbacks, and climate sensitivity. In V. Masson-Delmotte, P. Zhai, A. Pirani, S. L. Connors, C. Péan, S. Berger, et al. (Eds.), *Climate change 2021: The physical science basis. Contribution of working group i to the sixth assessment report of the intergovernmental panel on climate change* (pp. 923–1054). Cambridge University Press. <https://doi.org/10.1017/9781009157896.009>

Frankenberg, C., Thorpe, A. K., Thompson, D. R., Hulley, G., Kort, E. A., Vance, N., et al. (2016). Airborne methane remote measurements reveal heavy-tail flux distribution in four corners region. *Proceedings of the National Academy of Sciences of the United States of America*, 113(35), 9734–9739. <https://doi.org/10.1073/pnas.1605617113>

Gelaro, R., McCarty, W., Suárez, M. J., Todling, R., Molod, A., Takacs, L., et al. (2017). The modern-era retrospective analysis for research and applications, version 2 (MERRA-2). *Journal of Climate*, 30(14), 5419–5454. <https://doi.org/10.1175/JCLI-D-16-0758.1>

GHGSat. (2024). Greenhouse gas emissions monitoring. Retrieved from <https://www.ghgsat.com>

Girard, C., Plante, A., Desgagné, M., McTaggart-Cowan, R., Côté, J., Charron, M., et al. (2014). Staggered vertical discretization of the Canadian environmental multiscale (GEM) model using a coordinate of the log-hydrostatic-pressure type. *Monthly Weather Review*, 142(3), 1183–1196. <https://doi.org/10.1175/MWR-D-13-00255.1>

Global Modeling and Assimilation Office (GMAO). (2015). inst33dasmCp: MERRA-2 3D IAU State, Meteorology Instantaneous 3-hourly (p-coord, 0.625x0.5L42) version 5.12.4 [Dataset]. *Goddard Space Flight Center Distributed Active Archive Center (GSFC DAAC)*. Retrieved from <https://gmao.gsfc.nasa.gov/reanalysis/MERRA-2/>

Government of Canada. (2024). Government of Canada open government licence. Retrieved from <https://open.canada.ca/en/open-government-licence-canada>

Hamburg, S., Gautam, R., & Zavala-Araiza, D. (2022). MethaneSAT - A new tool purpose-built to measure oil and gas methane emissions from space (Conference paper). <https://doi.org/10.2118/210922-MS>

- He, Z., Gao, L., Liang, M., & Zeng, Z.-C. (2024). A survey of methane point source emissions from coal mines in Shanxi province of China using AHSI on board Gaofen-5B. *Atmospheric Measurement Techniques*, *17*(9), 2937–2956. <https://doi.org/10.5194/amt-17-2937-2024>
- Hersbach, H., Bell, B., Berrisford, P., Hirahara, S., Horányi, A., Muñoz-Sabater, J., et al. (2020). The ERA5 global reanalysis [Dataset]. *StI*, *146*(730), 1999–2049. <https://doi.org/10.1002/qj.3803>
- Hoffman, I., Malo, A., Mekarski, P., Yi, J., Zhang, W., Ek, N., et al. (2020). Mapping the deposition of C137s and I131 in north America following the 2011 Fukushima Daiichi Reactor accident. *Atmospheric Environment X*, *6*, 100072. <https://doi.org/10.1016/j.aeaoa.2020.100072>
- Jacob, D. J., Turner, A. J., Maasakkers, J. D., Sheng, J., Sun, K., Liu, X., et al. (2016). Satellite observations of atmospheric methane and their value for quantifying methane emissions. *Atmospheric Chemistry and Physics*, *16*(22), 14371–14396. <https://doi.org/10.5194/acp-16-14371-2016>
- Jacob, D. J., Varon, D. J., Cusworth, D. H., Dennison, P. E., Frankenberg, C., Gautam, R., et al. (2022). Quantifying methane emissions from the global scale down to point sources using satellite observations of atmospheric methane. *Atmospheric Chemistry and Physics*, *22*(14), 9617–9646. <https://doi.org/10.5194/acp-22-9617-2022>
- Jervis, D., McKeever, J., Durak, B. O. A., Sloan, J. J., Gains, D., Varon, D. J., et al. (2021). The GHGSat-D imaging spectrometer. *Atmospheric Measurement Techniques*, *14*(3), 2127–2140. <https://doi.org/10.5194/amt-14-2127-2021>
- Johnson, M. R., Conrad, B. M., & Tyner, D. R. (2023a). Creating measurement-based oil and gas sector methane inventories using source-resolved aerial surveys. *Communications Earth & Environment*, *4*(1), 139. <https://doi.org/10.1038/s43247-023-00769-7>
- Johnson, M. R., Conrad, B. M., & Tyner, D. R. (2023b). Origins of oil and gas sector methane emissions: On-site investigations of aerial measured sources. *Environmental Science and Technology*, *45*(6), 2484–2494. <https://doi.org/10.1021/acs.est.2c07318>
- Johnson, M. R., Tyner, D. R., Conley, S., Schwietzke, S., & Zavala-Araiza, D. (2017). Comparisons of airborne measurements and inventory estimates of methane emissions in the Alberta upstream oil and gas sector. *Environmental Science & Technology*, *51*(21), 13008–13017. <https://doi.org/10.1021/acs.est.7b03525>
- Lorente, A., Borsdorff, T., Butz, A., Hasekamp, O., van de Brugh, J., Schneider, A., et al. (2021). Methane retrieved from TROPOMI: Improvement of the data product and validation of the first 2 years of measurements. *Atmospheric Measurement Techniques*, *14*(1), 665–684. <https://doi.org/10.5194/amt-14-665-2021>
- Lu, X., Jacob, D. J., Wang, H., Maasakkers, J. D., Zhang, Y., Scarpelli, T. R., et al. (2022). Methane emissions in the United States, Canada, and Mexico: Evaluation of national methane emission inventories and 2010–2017 sectoral trends by inverse analysis of in situ (GLOBALVIEWplus CH₄ ObsPack) and satellite (GOSAT) atmospheric observations. *Atmospheric Chemistry and Physics*, *22*(1), 395–418. <https://doi.org/10.5194/acp-22-395-2022>
- Maasakkers, J. D., Varon, D. J., Elfarsdóttir, A., McKeever, J., Jervis, D., Mahapatra, G., et al. (2022). Using satellites to uncover large methane emissions from landfills. *Science Advances*, *8*(32), eabn9683. <https://doi.org/10.1126/sciadv.abn9683>
- MacKay, K., Lavoie, M., Bourlon, E., Atherton, E., O’Connell, E., Baillie, J., et al. (2021). Methane emissions from upstream oil and gas production in Canada are underestimated. *Scientific Reports*, *11*(1), 8041. <https://doi.org/10.1038/s41598-021-87610-3>
- Molod, A., Takacs, L., Suarez, M., Bacmeister, J., Song, I.-S., & Eichmann, A. (2012). The GEOS-5 atmospheric general circulation model: Mean climate and development from MERRA to Fortuna. Retrieved from <https://ntrs.nasa.gov/citations/20120011790>
- NASA Global Modeling and Assimilation Office. (2023). Goddard earth observing system forward processing forecast data [Dataset]. Retrieved from https://gmao.gsfc.nasa.gov/GMAO_products/NRT_products.php
- Nassar, R., Hill, T. G., McLinden, C. A., Wunch, D., Jones, D. B. A., & Crisp, D. (2017). Quantifying CO₂ emissions from individual power plants from space. *Geophysical Research Letters*, *44*(19), 10045–10053. <https://doi.org/10.1002/2017GL074702>
- NOAA. (2020). ETOPO 2022 15 arc-second global relief model [Dataset]. <https://doi.org/10.25921/fd45-gt74>
- NOAA. (2024). Global monitoring laboratory. Retrieved from <https://gml.noaa.gov/dv/iadv/graph.php>
- Pommier, M., McLinden, C. A., & Deeter, M. (2013). Relative changes in CO emissions over megacities based on observations from space. *Geophysical Research Letters*, *40*(14), 3766–3771. <https://doi.org/10.1002/grl.50704>
- Rogers, C. D. (2000). Inverse methods for atmospheric sounding: Theory and practice.
- Schaaf, C. B., Gao, F., Strahler, A. H., Lucht, W., Li, X., Tsang, T., et al. (2002). First operational BRDF, albedo nadir reflectance products from MODIS. *Remote Sensing of Environment*, *83*(1), 135–148. [https://doi.org/10.1016/S0034-4257\(02\)00091-3](https://doi.org/10.1016/S0034-4257(02)00091-3)
- Schaaf, C. B., & Wang, Z. (2015). MCD43C3 MODIS/Terra+Quia BRDF/albedo albedo daily L3 global 0.05Deg CMG V006 [Dataset]. NASA EOSDIS Land Processes Distributed Active Archive Center. <https://doi.org/10.5067/MODIS/MCD43C3.061>
- Tyner, D. R., & Johnson, M. R. (2021). Where the methane is—Insights from novel airborne LiDAR measurements combined with ground survey data. *Environmental Science & Technology*, *55*(14), 9773–9783. <https://doi.org/10.1021/acs.est.1c01572>
- Varon, D. J., Jacob, D. J., McKeever, J., Jervis, D., Durak, B. O. A., Xia, Y., & Huang, Y. (2018). Quantifying methane point sources from fine-scale satellite observations of atmospheric methane plumes. *Atmospheric Measurement Techniques*, *11*(10), 5673–5686. <https://doi.org/10.5194/amt-11-5673-2018>
- Yoshida, Y., Ota, Y., Eguchi, N., Kikuchi, N., Nobuta, K., Tran, H., et al. (2011). Retrieval algorithm for CO₂ and CH₄ column abundances from short-wavelength infrared spectral observations by the greenhouse gases observing satellite. *Atmospheric Measurement Techniques*, *4*(4), 717–734. <https://doi.org/10.5194/amt-4-717-2011>
- Zavala-Araiza, D., Herndon, S. C., Roscioli, J. R., Yacovitch, T. I., Johnson, M. R., Tyner, D. R., et al. (2018). Methane emissions from oil and gas production sites in Alberta, Canada. *Elementa: Science of the Anthropocene*, *6*, 27. <https://doi.org/10.1525/elementa.284>